

1 **New insight into the formation and aging processes of organic**  
2 **aerosol from positive matrix factorization (PMF) analysis of**  
3 **ambient FIGAERO-CIMS thermograms**

4 Mingfu Cai<sup>1,2,3</sup>, Bin Yuan<sup>2,3</sup>, Weiwei Hu<sup>4,5\*</sup>, Ye Chenshuo<sup>6</sup>, Shan Huang<sup>2,3</sup>, Suxia  
5 Yang<sup>7</sup>, Wei Chen<sup>4</sup>, Yuwen Peng<sup>2,3</sup>, Zhaoxiong Deng<sup>2,3</sup>, Jun Zhao<sup>8†</sup>, Duohong Chen<sup>9</sup>,  
6 Jiaren Sun<sup>1</sup>, Min Shao<sup>2,3</sup>

7 <sup>1</sup>Guangdong Province Engineering Laboratory for Air Pollution Control, Guangdong Provincial Key  
8 Laboratory of Water and Air Pollution Control, South China Institute of Environmental Sciences, MEE,  
9 Guangzhou 510655, China

10 <sup>2</sup>Institute for Environmental and Climate Research, Jinan University, Guangzhou 511443, China

11 <sup>3</sup>Guangdong-Hongkong-Macau Joint Laboratory of Collaborative Innovation for Environmental  
12 Quality, Jinan University, Guangzhou 510632, China

13 <sup>4</sup> State Key Laboratory of Advanced Environmental Technology, Guangzhou Institute of Geochemistry,  
14 Chinese Academy of Sciences, Guangzhou, 510640, China

15 <sup>5</sup> Guangdong-Hong Kong-Macao Joint Laboratory for Environmental Pollution and Control,  
16 Guangzhou Institute of Geochemistry, Chinese Academy of Science, Guangzhou, China

17 <sup>6</sup> Guangdong Provincial Academy of Environmental Science, Guangzhou, 510045, China

18 <sup>7</sup> Guangzhou Research Institute of Environment Protection Co.,Ltd, Guangzhou 510620, China

19 <sup>8</sup>School of Atmospheric Sciences, Guangdong Province Key Laboratory for Climate Change and  
20 Natural Disaster Studies, and Institute of Earth Climate and Environment System, Sun Yat-sen  
21 University, Zhuhai 519082, China

22 <sup>9</sup>Guangdong Environmental Monitoring Center, Guangzhou 510308, China

23 <sup>†</sup>Deceased, 10/2024

24

25 Correspondence to: Weiwei Hu (weiweihu@gig.ac.cn)

26

27        **Abstract**

28        Secondary organic aerosol (SOA) is an important component of organic aerosol (OA), yet its  
29        atmospheric evolution and impacts on volatility remain poorly understood. In this study, we  
30        investigated the volatility of different types of SOA at a downwind site of the Pearl River Delta  
31        (PRD) region in the fall of 2019, using a time-of-flight chemical ionization mass spectrometer  
32        coupled with a Filter Inlet for Gases and Aerosol (FIGAERO-CIMS). Positive matrix factorization  
33        (PMF) analysis was performed on the thermogram data of organic compounds (referred as  
34        FIGAERO-OA) measured by the FIGAERO-CIMS. Eight factors were resolved, including six  
35        daytime chemistry related factors, a biomass burning related factor (BB-LVOA, 10% of the  
36        FIGAERO-OA), and a nighttime chemistry related factor (Night-LVOA, 15%) along with their  
37        corresponding volatility. Day-HNO<sub>x</sub>-LVOA (12%) and Day-LNO<sub>x</sub>-LVOA (11%) were mainly  
38        formed through gas-particle partitioning. Increasing NO<sub>x</sub> levels mainly affected SOA formation  
39        through gas-particle partitioning, suppressing the formation of low-volatile organic vapors, and thus  
40        promoting the formation of relatively high volatile OA with a higher N:C ratio. Two aged OA factors,  
41        Day-aged-LVOA (16%) and Day-aged-ELVOA (11%), were attributed to daytime photochemical  
42        aging of pre-existing OA. In addition, the daytime formation of Day-urban-LVOA (16%) and Day-  
43        urban-ELVOA (7%) could only be observed in the urban plume. Results show that both gas-particle  
44        partitioning (36%) and photochemical aging (30%) accounted for a major fraction in FIGAERO-  
45        OA in the afternoon during the urban air masses period, especially for high-NO<sub>x</sub>-like pathway  
46        (~21%). In general, the six daytime OA factors collectively explain the majority (82%) of daytime  
47        SOA identified by an aerosol mass spectrometer (AMS). While BB-LVOA and Night-LVOA  
48        accounted for 13% of biomass burning OA and 48% of nighttime chemistry OA observed by AMS,  
49        respectively. Our PMF analysis also demonstrated that the the highly oxygenated OA and  
50        hydrocarbon-like OA cannot be identified with FIGAERO-CIMS in this study. In summary, our  
51        results show that the volatility of OA is strongly governed by its formation pathways and subsequent  
52        atmospheric aging processes.

53

54 **1. Introduction**

55 Secondary organic aerosols (SOA), a major component of fine particular matter (PM<sub>2.5</sub>) in  
56 China (Zhou et al., 2020), exert profound influences on climate change, human health, and air  
57 quality (Arias et al., 2021; Apte et al., 2018; Huang et al., 2014). Despite notable reductions in  
58 primary emission in recent years, SOA has emerged as an increasingly crucial factor in haze  
59 formation in China (Zhang et al., 2018). However, accurately modeling SOA from current chemical  
60 models is still challenging, largely attributed to our limited understanding of its formation  
61 mechanisms (Charan et al., 2019; Matsui et al., 2009; Lu et al., 2020). Thus, there is a crucial need  
62 for a comprehensive understanding of SOA formation and aging processes in the ambient  
63 environment.

64 Positive matrix factorization (PMF) has been widely used to apportion the contribution of  
65 primary and secondary sources to organic aerosol (OA) (Chen et al., 2014; Chen et al., 2021a; Ou  
66 et al., 2023; Tian et al., 2016). For the input of OA, the matrix of time serial spectral of OA measured  
67 by the Aerodyne Aerosol Mass Spectrometers (AMS) or Aerosol Chemical Speciation Monitor  
68 (ACSM) was usually applied (Uchida et al., 2019; Canonaco et al., 2013). Based on this approach,  
69 various primary OA (POA) components such as, hydrocarbon-like OA (HOA, associated with traffic  
70 emission), biomass burning OA (BBOA), cooking OA (COA), and secondary OA (SOA) with  
71 different oxidation levels are broadly identified in field measurements (Zhang et al., 2012; Jimenez  
72 et al., 2009; Huang et al., 2010; Qin et al., 2017; Guo et al., 2020; Huang et al., 2018; Al-Naiema et  
73 al., 2018). OA factors are generally distinguished according to their features on mass spectral and  
74 time series (Ulbrich et al., 2009; Lee et al., 2015). However, the electric ionization sources (70ev),  
75 together with thermal decomposition at 600C, lead to strongly fragmented ions detected in  
76 AMS/ACSM. These fragmented ions lack parent molecular information, thus hindering the ability  
77 to further attribute OA factors to more specific sources, thereby limiting our understanding of SOA  
78 formation pathways and aging mechanisms in ambient environments. To overcome this challenge,  
79 applying PMF analysis of molecular-level datasets is needed for refining SOA source apportionment.  
80 Recently, chemical ionization mass spectrometer coupled with the Filter Inlet for Gases and  
81 Aerosols (FIGAERO-CIMS) has been increasingly employed for the molecular-level  
82 characterization of oxygenated organics compounds in the gas and particle phase (Ye et al., 2021;

83 Thornton et al., 2020). Using this approach, Ye et al. (2023) employed PMF analysis to FIGAERO-  
84 CIMS data sets and found that low-NO-like pathway had a significant contribution to SOA  
85 formation in urban area.

86 Volatility, an important property of organic compounds, is frequently described as saturation  
87 mass concentration ( $C^*$ , Donahue et al., 2006). The volatility of organic compounds is closely  
88 related to its chemical characteristics, including oxidate state, number of carbons, and functional  
89 groups (Donahue et al., 2012; Donahue et al., 2011; Ren et al., 2022). The gas–particle partitioning  
90 behavior of organic compounds is largely governed by their volatility, and thus strongly influence  
91 the formation of SOA (Nie et al., 2022). Moreover, chemical processes occurring in the particle  
92 phase can alter the volatility of organic compounds. For example, high molecular weight organic  
93 compounds can form through accretion reactions, leading to a reduction in volatility (Barsanti and  
94 Pankow, 2004; Jenkin, 2004; Kroll and Seinfeld, 2008). In addition, particle phase organic  
95 compounds can be oxidized by atmospheric oxidants (e.g.,  $O_3$ , OH, and  $NO_3$ ), which can also alter  
96 the chemical characteristic and volatility (Rudich et al., 2007; Walser et al., 2007). Thus, the  
97 variation of volatility can provide valuable information about the formation and aging processes of  
98 OA. Graham et al. (2023) found that SOA from  $NO_3$  oxidation of  $\alpha$ -pinene or isoprene had a higher  
99 volatility than it from  $\beta$ -caryophyllene. Hildebrandt Ruiz et al. (2015) demonstrated that exposure  
100 to different OH levels could lead to a large variation in SOA volatility.

101 However, linking OA volatility directly to its chemical characteristics and sources remains  
102 challenging. A thermodenuder (TD) coupled with an AMS has been employed to investigate the  
103 volatility of OA from different sources (Louvaris et al., 2017). Xu et al. (2021) estimated the  
104 volatility of different PMF OA factors in the North China Plain and reported that RH level could  
105 alter both the formation pathway and volatility of more oxidized oxygenated OA. Feng et al. (2023)  
106 reported the much lower OA volatility from out plumes of North China plain than results obtained  
107 in the urban areas, signifying the aging impact on OA volatility. Nevertheless, owing to the  
108 operational principle of AMS, it is still difficult to obtain molecular information of organic  
109 compounds at different volatilities. In contrast, the FIGAERO-CIMS provides not only molecular-  
110 level measurements but also thermal desorption profiles (thermograms) for each detected compound.  
111 The temperature of the peak desorption signal ( $T_{max}$ ) of a specific compound is typically correlated  
112 with its volatility (Lopez-Hilfiker et al., 2014), enabling direct connects between the volatility and

113 organic molecular (Ren et al., 2022). Huang et al. (2019) analysis the ambient particles filter samples  
114 collected in different seasons with FIGAERO-CIMS and reported a lower volatility of oxygenated  
115 OA in winter, partly due to higher O:C. Buchholz et al. (2020) utilized PMF analysis of FIGAERO-  
116 CIMS thermogram data sets to investigate physicochemical property of laboratory-generated SOA  
117 particles.

118 To comprehensively investigate the evolution of OA and its relationship with volatility in  
119 ambient environment, we employed a FIGAERO-CIMS along with other online instruments to gain  
120 a comprehensive understanding of the variation in SOA volatility within urban plumes in the Pearl  
121 River Delta (PRD) region during the fall of 2019. PMF analysis was performed on thermograms  
122 data obtained from the FIGAERO-CIMS. By combining the source apportionment of thermogram  
123 organic aerosol (OA) with corresponding volatility information, we investigated the potential  
124 formation pathway and influencing factors of SOA in the urban downwind region.

## 125 **2. Measurement and Method**

### 126 **2.1 Field Measurements**

127 We conducted a field campaign at the Heshan supersite in the PRD region from September 29  
128 to November 17, 2019. Considering the integrity of the measurements, we focus primarily on the  
129 period from October 16 to November 16, 2019 in this study. The measurement site was located in a  
130 rural area surrounded by farms and villages (at 22°42'39. 1"N, 112°55'35.9"E, with an altitude of  
131 about 40 m), situated to the southwest of the PRD region. All online instruments were placed in air-  
132 conditioned rooms on the top floor of the supersite building.

133 A FIGAERO-CIMS, coupled with an X-ray source, was used to measure organic compounds  
134 in both the gas- and particle-phase, utilizing  $I^-$  as the chemical ionization reagent. The instrument  
135 operated on one-hour cycle by switching between two modes (sampling mode and desorption mode)  
136 for measuring gas- and particle-phase oxygenated organic molecules. In the sampling mode,  
137 ambient gas was measured in the first 21 minutes, followed by a 3-min zero air background, while  
138 the  $PM_{2.5}$  sample was collected on a PTFE membrane filter for 24 minutes. Then, the instrument  
139 was switched to the desorption mode, in which the collected particles were desorbed using heated  
140  $N_2$ . The temperature of the  $N_2$  was increased from approximately 25°C to 175°C over a 12-minute  
141 period, and then held at 175°C for an additional 24 minutes. Calibration of a few chemicals was

142 conducted in the laboratory. For the remaining organic species, a voltage scanning method was used  
143 to determine their sensitivities (referred to as semi-quantified species) (Ye et al., 2021; Iyer et al.,  
144 2016; Lopez-Hilfiker et al., 2016). The detailed operation settings, data processing, and calibration  
145 can be found in Cai et al. (2023) and Ye et al. (2021).

146 A soot particle aerosol mass spectrometer (SP-AMS, Aerodyne Research, Inc., USA) was used  
147 to measure the chemical composition of PM<sub>1</sub> particles, including nitrate, sulfate, ammonium,  
148 chloride, black carbon, and OA. More details on the quantification using ionization efficiency,  
149 composition dependent collection efficiency, data analysis, and source apportionment of OA from  
150 AMS data (defined as AMS-OA) could be found in Kuang et al. (2021) and Cai et al. (2024). In  
151 brief, AMS-OA consisted of two primary OA factors and four secondary OA factors. The primary  
152 OA factors include hydrocarbon-like OA (HOA, 11%) and biomass burning OA (BBOA, 20%),  
153 which were mainly contributed by traffic and cooking emissions and biomass burning combustion,  
154 respectively. For SOA factors, biomass burning SOA (BBSOA, 17%) was likely formed through  
155 oxidation of biomass burning emission; less oxidized oxygenated OA (LO-OOA, 24%), which  
156 results from strong daytime photochemical processes; more oxidized oxygenated OA (MO-OOA,  
157 17%), related to regional transport; and nighttime-formed OA (Night-OA, 11%) which was  
158 associated with nighttime chemistry.

159 Trace gases such as O<sub>3</sub> and NO<sub>x</sub> were measured by gas analyzers (model 49i and 42i, Thermo  
160 Scientific, US). Meteorological parameters, including wind speed and wind direction, were  
161 measured by a weather station (Vantage Pro 2, Davis Instruments Co., US).

## 162 **2.2 Methodology**

163 Positive matrix factorization (PMF) is a widely used tool for source apportionment of long  
164 timeseries data (Paatero and Tapper, 1994). In the desorption mode, the particulate organic  
165 compounds are thermo-desorbed and simultaneously measured by the FIGAERO-CIMS. Organic  
166 molecules with different volatility were characterized by thermograms (desorption signals vs  
167 temperature of N<sub>2</sub>). Here, we performed PMF analysis to the thermogram data of organic  
168 compounds measured by the FIGAERO-CIMS (FIGAERO-OA) using the Igor-based PMF  
169 Evaluation Tool (PET, v3.01, Ulbrich et al., 2009), which can be expressed as follows:

$$170 \quad \mathbf{X} = \mathbf{GF} + \mathbf{E} \quad (1)$$

171 where  $\mathbf{X}$  is the thermogram organic compound data measured by the FIGAERO-CIMS. which

172 can be decomposed into two matrices  $\mathbf{G}$  and  $\mathbf{F}$ . The matrix  $\mathbf{G}$ ,  $\mathbf{F}$ , and  $\mathbf{E}$  contain the factor time series,  
173 factor mass spectra, and the residuals between the measured data and the reconstructed data.

174 The raw normalized count per second (NCPS) thermogram data with a time resolution of 1s  
175 was averaged to a 20s-time grid, and then was background-corrected by subtracting linearly  
176 interpolated background thermogram signals. For each scan, only the data points when the  
177 desorption temperature increased were used as input data (corresponding to 25°C to 170 °C, 1-70  
178 data points in this study, Fig. S1), since the main information lies during the species desorbing from  
179 the FIGAERO filter (Fig. S1, Buchholz et al., 2020). Then, we combined data from separate  
180 thermogram scans (without background scans) to a larger input data set.

181 To perform the PMF analysis, a data uncertainty matrix ( $S_{i,j}$ ) is needed, where the  $i$  and  $j$   
182 represents the index of ions and data points, respectively. According to Buchholz et al. (2020), the  
183 uncertainty was assumed to be constant for each individual thermogram scan (constant error  
184 scheme). The  $S_{i,j}$  of a specific thermogram scan can be determined by the following equation:

$$185 \quad S_{i,j} = \sigma \quad (2)$$

186 For each thermogram scan, the last 20 data points are assumed to be in steady state. Thus, the  
187  $\sigma_{noise}$  was calculated as the median of the standard deviation of the residual ( $res_{i,j}$ ), which can be  
188 obtained from the difference between the data points ( $Data_{i,j}$ ) and the corresponding linear fitted  
189 value ( $FittedData_{i,j}$ ) for the measured data points (Fig. S2):

$$190 \quad res_{i,j} = Data_{i,j} - FittedData_{i,j} \quad (3)$$

$$191 \quad \sigma = median(stdev(res_{i,j})) \quad (4)$$

192 Due to the large volume of the data matrix (59500×1028) exceeding the processing capacity  
193 of the PET, we had to divide the data matrix into three parts and performed PMF analysis separately.

194 An eight-factor solution was selected for each part based on  $Q/Q_{exp}$  behavior and factor  
195 interpretability (Fig. S3 to S6). To assess factor consistency, the mass spectra of resolved factors  
196 were compared across different parts, showing strong correlations ( $R>0.9$ ) for the each factor (Fig.  
197 S7 and S8). Weaker correlations during the early campaign period (2 to 5 October) likely reflect  
198 changes in dominant OA sources under different meteorological conditions (Fig. S8 and S9). After  
199 excluding this period, consistent factor profiles were obtained and combined for further analysis.  
200 Detailed evaluations are provided in the Section S1. An eight-factor solution was selected for each  
201 part based on  $Q/Q_{exp}$  behavior and factor interpretability (Fig. S3 to S6). To assess factor consistency,

Formatted: Subscript

202 the mass spectra of resolved factors were compared across different parts, showing strong  
203 correlations ( $R>0.9$ ) for the each factor (Fig. S7 and S8). Weaker correlations during the early  
204 campaign period (2 to 5 October) likely reflect changes in dominant OA sources under different  
205 meteorological conditions (Fig. S8 and S9). After excluding this period, consistent factor profiles  
206 were obtained and combined for further analysis. Detailed evaluations are provided in the Section  
207 **SI**.

208 Since input data sets of PMF analysis were the NCPS data, the signal of each thermograms  
209 factor was a combination of NCPS values of different ions. Thus, it is necessary to convert the signal  
210 of these factors into mass concentrations, which would increase the representativeness of the  
211 thermogram PMF results. The NCPS of a specific ion was linearly correlated with the corresponding  
212 mass concentration. Thus, for a signal running cycle (a thermogram scan), the mass concentration  
213 of a specific thermograms OA factor  $k$  ( $M_k$ ) can be estimated as:

$$214 M_k = \sum_i \left( \frac{\sum_j Signal_{j,k} \cdot Profile_{i,k}}{\sum_j NCPS_{j,i}} \cdot m_i \right) \quad (75)$$

215 where  $i$  and  $j$  represent the index of species and data points; the  $Signal_{j,k}$  is the signal of a  
216 thermograms OA factor  $k$  at a data index  $j$ ; the  $Profile_{i,k}$  represents the fraction of signal of factor  
217  $k$  and ion  $i$ ; the  $NCPS_{j,i}$  is the NCPS of species  $i$  at a data index  $j$ ; and  $m_i$  is the mass concentration  
218 of species  $i$  in the particle-phase measured by the FIGAERO-CIMS.

219 For a specific organic compound, the temperature of the peak desorption signal ( $T_{max}$ ) has a  
220 nearly linear relationship with the logarithm of saturation vapor pressure ( $P_{sat}$ ) of the respective  
221 organic compound (Lopez-Hilfiker et al., 2014):

$$222 \ln(P_{sat}) = aT_{max} + b \quad (86)$$

223 where  $a$  and  $b$  are fitting coefficients.  $P_{sat}$  can be converted to saturation vapor concentration  
224 ( $C^*$ ,  $\mu\text{g m}^{-3}$ ) by following equation:

$$225 C^* = \frac{P_{sat} M_w}{RT} 10^6 \quad (79)$$

226 where  $M_w$  is the average molecular weight of the organic compound (determined by the FIGAERO-  
227 CIMS),  $R$  is the gas constant ( $8.314 \text{ J mol}^{-1} \text{ K}^{-1}$ ), and  $T$  is the thermodynamic temperature (298.15  
228 K). The fitting parameters of  $a$  and  $b$  were calibrated by a series of polyethylene glycol (PEG 5-8)  
229 compounds before the campaign. PEG standards (dissolved in acetonitrile) were atomized using a  
230 homemade atomizer, and the resulting particles were size-classified by a differential mobility

231 analyzer (DMA; model 3081L, TSI Inc.) to target diameters of 100 and 200 nm. The size-selected  
232 particles were then split into two flows: one directed go to a CPC (3775, TSI) for the measurements  
233 of number concentration, and the other to the FIGAERO-CIMS particle inlet. The collected mass  
234 by CIMS was calculated based on the particle diameter, number concentration, FIGAERO-CIMS  
235 inlet flow rate, and collection time. The details of the calibration experiments and selection of fitting  
236 coefficients (a and b) can be found in table S1 and Cai et al. (2024). In this study, the fitting  
237 parameters (a=-0.206 and b=3.732) were chosen, as the mass loading (407 ng) and diameter (200  
238 nm) are closest to the ambient samples, since the collected mass loading centered at about 620 ng  
239 and the particle volume size distribution (PVSD) centered at about 400 nm (Cai et al., 2024). The  
240 fitting parameters *a* and *b* was calibrated by a series of polyethylene glycol (PEG 5-8) compounds  
241 before the campaign. The details of the calibration experiments and selection of fitting coefficients  
242 (*a* and *b*) can be found in table S1 and Cai et al. (2024). In this study, the fitting parameters (*a*=  
243 0.206 and *b*=3.732) was chosen, as the mass loading (407 ng) and diameter (200 nm) are closest to  
244 the ambient samples (Cai et al., 2024). It was worth noting that the volatility range of PEG 5-8 (-  
245  $1.73 \leq \log_{10} C^* \leq 3.34 \text{ } \mu\text{g m}^{-3}$ ) may not fully represent the volatility of ambient organic aerosol,

246 particularly nitrogen-containing and highly oxygenated compounds that can exhibit much lower  
247 volatility ( $\log_{10} C^* \leq -2 \text{ } \mu\text{g m}^{-3}$ , Ren et al., 2022; Chen et al., 2024). At present, saturation vapor  
248 pressure data for PEG standards are only available up to PEG-8 (Krieger et al., 2018). Ylisirniö et  
249 al. (2021) demonstrated that different extrapolation approaches for estimating the volatility of  
250 higher-order PEGs can lead to substantial discrepancies in calibration results, and they strongly  
251 recommended that higher-order PEGs should only be used to extend the volatility calibration range  
252 once their saturation vapor pressures are accurately determined. Very recently, Ylisirniö et al. (2025)  
253 derived saturation vapor pressures for higher-order PEGs up to PEG-15 and demonstrated that  
254 extending FIGAERO-CIMS calibration to much lower volatilities is feasible, but also showed that  
255 different estimation approaches for higher-order PEGs can lead to large discrepancies, highlighting  
256 substantial uncertainties when extrapolating volatility calibration beyond PEG-8. Therefore,  
257 uncertainties may remain in the calibration of low-volatility OA, and further calibration experiments  
258 using complementary techniques are highly recommended. Therefore, uncertainties may remain in  
259 the calibration of low-volatility OA, and further calibration experiments using complementary  
260 techniques are highly recommended.

261 **3 Results**

262 **3.1 Overview of FIGAERO-OA factors**

263 In this study, the average mass concentration of FIGAERO-OA was about  $5.3 \pm 2.4 \mu\text{g m}^{-3}$ . The  
264 thermogram data sets of FIGAERO-OA were analyzed with PMF and mass concentration of each  
265 factor was estimated based on eq. (75), which provide volatility and mass concentration information  
266 of OA originating from different formation pathways. An 8-factor solution was chosen to explain  
267 the thermogram of FIGAERO-OA. These factors included six associated with daytime  
268 photochemical reactions, one related to biomass-burning, and one factor contributed by nighttime  
269 chemistry. The diurnal variation, mass spectra, and thermograms of these factors can be found in  
270 Fig. S6S9. The estimated volatility ( $\log_{10} C^*$ ),  $T_{max}$ , and elemental information of all factors are  
271 shown in table 1. Given that the thermogram data can provide volatility information of organic  
272 compounds, the identified OA factors were categorized based on their potential formation pathway,  
273 volatility, and correlation with AMS PMF factors (Table 1 and Fig. S7S10). For example, if the  
274 PMF factor with a  $T_{max}$  located in the ranges of low volatile organic compounds (LVOC,  
275 approximately corresponding to 78.8 °C to 112.3 °C then Fig. 1), this factor will be named after low  
276 volatility OA (LVOA). For the factors whose  $T_{max}$  is above 112.3 °C, extremely low volatility  
277 (ELVOA) will be named.

278 The six daytime chemistry related factors include a low volatility OA factor likely formed  
279 under high NO<sub>x</sub> condition (Day-HNO<sub>x</sub>-LVOA, 12%), a low volatility factor contributed by gas-  
280 particle partitioning (Day-LNO<sub>x</sub>-LVOA, , 11%), a low volatility and an extremely low volatility  
281 factor originating from the daytime aging process (Day-aged-LVOA and Day-aged-ELVOA, 16%  
282 and 11% respectively), and a low volatility and an extremely low volatility factors related to urban  
283 air masses (Day-urban-LVOA and Day-urban-ELVOA, 16% and 7%, respectively). These daytime  
284 factors accounted for about 76.4% of the total mass of FIGAERO-OA and demonstrated distinct  
285 daytime peak. The total mass of daytime FIGAERO-OA factors showed a strong positive correlation  
286 with LO-OOA in AMS-OA ( $R=0.86$ ), which was attributed to photochemical reactions (Fig.  
287 S7S10a).

288 Both Day-HNO<sub>x</sub>-LVOA and Day-LNO<sub>x</sub>-LVOA reached their peak values at about 14:00 LT  
289 (Fig. 1 a1 and b1), implying strong photochemical production. Day-HNO<sub>x</sub>-LVOA had the highest

N:C (0.06) and the lowest oxidation state ( $\overline{OS}_c = -0.01$ ), which could be attributed to the “high NO<sub>x</sub>” formation pathway. It was also supported by significant positive correlation (R=0.93-0.94) with particulate phase nitrogen-containing organic compounds (e.g., C<sub>4</sub>H<sub>5</sub>NO<sub>6</sub>, C<sub>8</sub>H<sub>11</sub>NO<sub>8</sub>, and C<sub>8</sub>H<sub>11</sub>NO<sub>9</sub>). Previous studies found that high NO<sub>x</sub> concentration can suppress the production of molecules with a high oxidation degree (Rissanen, 2018; Praske et al., 2018), which could explain the low  $\overline{OS}_c$  value (-0.01) and relative high volatility ( $\log_{10} \overline{C^*} = -0.98$ ) found for Day-HNO<sub>x</sub>-LVOA. Day-LNO<sub>x</sub>-LVOA had a higher  $\overline{OS}_c$  (0.18) and lower  $\log_{10} \overline{C^*}$  (-2.71) than Day-HNO<sub>x</sub>-LVOA, consistent with that Day-LNO<sub>x</sub>-LVOA was composed of smaller and more oxidized non-nitrogen containing compounds (e.g., C<sub>2</sub>H<sub>2</sub>O<sub>3</sub>, C<sub>3</sub>H<sub>4</sub>O<sub>3</sub>, C<sub>4</sub>H<sub>6</sub>O<sub>4</sub>, and C<sub>6</sub>H<sub>8</sub>O<sub>4</sub>). Noting that C2-C3 group could originate from the decomposition of larger molecules during thermal desorption, since the thermogram of C<sub>2</sub>H<sub>2</sub>O<sub>3</sub> and C<sub>3</sub>H<sub>4</sub>O<sub>3</sub> demonstrated a bimodal distribution (Fig. 4-9 ab3). Figure S12 b and d further examine the contribution of all FIGAERO factors to the signals of C<sub>2</sub>H<sub>2</sub>O<sub>3</sub> and C<sub>3</sub>H<sub>4</sub>O<sub>3</sub>. One mode, peaking in the LVOC range, was primarily associated with Day-LNO<sub>x</sub>-LVOA, and a second mode, peaking in the ELVOC range, was dominated by Day-aged-ELVOA. These results indicates that these two low molecular weight species are likely decomposition products of at least two distinct classes of higher molecular weight organic compounds, and C<sub>2</sub>H<sub>2</sub>O<sub>3</sub> and C<sub>3</sub>H<sub>4</sub>O<sub>3</sub> had a relatively high  $T_{max}$  (Fig. S9a).

307 Additionally, we identified two aged OA factors (Day-aged-LVOA and Day-aged-ELVOA)  
 308 with an afternoon peak at about 18:00 LT (Fig. 1 c1 and d1), which may be derived from the aging  
 309 transformation of preexisting organic aerosols via daytime photochemical reactions. These aged  
 310 factors exhibited the highest  $\overline{OS_c}$  (0.35 and 0.40) and relatively low volatility with a  $\log_{10} \overline{C}^*$  of -  
 311 2.02 and -4.80, respectively. Day-aged-LVOA was featured with a series of C<sub>4</sub>-C<sub>8</sub> oxygenated  
 312 compounds (e.g., C<sub>4</sub>H<sub>6</sub>O<sub>5</sub>, C<sub>5</sub>H<sub>8</sub>O<sub>5</sub>, C<sub>6</sub>H<sub>10</sub>O<sub>5</sub>, C<sub>7</sub>H<sub>10</sub>O<sub>5</sub>, and C<sub>8</sub>H<sub>12</sub>O<sub>5</sub>). In contrast, Day-aged-  
 313 ELVOA had a higher fraction of smaller molecules (e.g., C<sub>2</sub>H<sub>4</sub>O<sub>3</sub> and C<sub>3</sub>H<sub>6</sub>O<sub>3</sub>, Fig. 1d2). Chen et  
 314 al. (2021b) found that low molecular weight carboxylic acids (LMWCA) could form through SOA  
 315 aging processes and report a strong correlation ( $R^2=0.90$ ) between LMWCA and highly oxygenated  
 316 OA. However, C<sub>2</sub>H<sub>4</sub>O<sub>3</sub> and C<sub>3</sub>H<sub>6</sub>O<sub>3</sub> had a weak correlation ( $R=0.49$  and 0.13) with MO-OOA  
 317 resolved from AMS (Fig. S11). In addition, the  $T_{max}$  of C<sub>2</sub>H<sub>4</sub>O<sub>3</sub> and C<sub>3</sub>H<sub>6</sub>O<sub>3</sub> located in the ELVOC  
 318 range and C<sub>2</sub>H<sub>4</sub>O<sub>3</sub> showed thermogram profiles similar to that of has a similar thermogram with  
 319 Day-aged-ELVOA (Fig. S9S12a). The thermogram signal of C<sub>2</sub>H<sub>4</sub>O<sub>3</sub> and C<sub>3</sub>H<sub>6</sub>O<sub>3</sub> was mainly

<b>Formatted:</b> Not Highlight
<b>Formatted:</b> Not Highlight
<b>Formatted:</b> Not Superscript/ Subscript, Not Highlight
<b>Formatted:</b> Not Highlight
<b>Formatted:</b> Not Highlight
<b>Formatted:</b> Not Highlight
<b>Formatted:</b> Not Highlight
<b>Formatted:</b> Not Highlight
<b>Formatted:</b> Font colour: Auto
<b>Formatted:</b> Font: (Asian) +Body Asian (等线)
<b>Formatted:</b> Highlight

**Formatted:** Subscript

**Formatted:** Subscript

**Formatted:** Subscript

320 contributed by Day-aged-ELVOA (Fig. S12 c and e), supporting the interpretation that these  
321 species are more likely decomposition products of low volatility organic compounds rather than  
322 being directly formed through atmospheric aging processes, supporting  $C_2H_4O_2$  was more likely  
323 decomposition product of low volatile organic compounds rather than directly formed through  
324 aging process.

325 Two urban air masses-related OA factors (Day-urban-LVOA and Day-urban-ELVOA) were  
326 identified, which would be discussed in the following section. Day-urban-LVOA demonstrated  
327 comparable  $\overline{OS}_c$  (0.08), O:C (0.80) and volatility (-0.90) to Day-HNO<sub>x</sub>-LVOA (-0.01, 0.75, and -  
328 0.98, respectively), but show a higher fraction of non-N-containing molecules (e.g., C<sub>4</sub>H<sub>6</sub>O<sub>4</sub>,  
329 C<sub>5</sub>H<sub>6</sub>O<sub>4</sub>, C<sub>5</sub>H<sub>8</sub>O<sub>5</sub>, and C<sub>7</sub>H<sub>10</sub>O<sub>5</sub>) and a reduced N:C ratio (Table 1). However, the oxidation state  
330 ( $\overline{OS}_c$ ) of Day-HNO<sub>x</sub>-LVOA (-0.01) was significantly lower than that of Urban-LVOA (0.08),  
331 accompanied by a relatively higher N:C (0.06 vs 0.04). Despite its lower oxidation state, the  
332 volatility of Day-HNO<sub>x</sub>-LVOA is comparable to that of Day-urban-LVOA, likely due to its higher  
333 nitrogen content. Organic nitrates generally exhibit lower volatility than hydroxylated products with  
334 the same carbon number (Donahue et al., 2011; Ren et al., 2022). Day-urban-ELVOA had the  
335 lowest volatility ( $\log_{10} C^* = -7.18$ ) but an  $\overline{OS}_c$  (0.27) lower than Day-aged-ELVOA (0.34) and  
336 composed of oxygenated compounds (e.g., C<sub>8</sub>H<sub>10</sub>O<sub>5</sub>, C<sub>7</sub>H<sub>8</sub>O<sub>5</sub>, C<sub>6</sub>H<sub>8</sub>O<sub>4</sub>, and C<sub>5</sub>H<sub>6</sub>O<sub>4</sub>). The  
337 thermogram of Day-aged-ELVOA demonstrates bimodal distribution (peaked at LVOC and  
338 ELVOC range) and had a highest  $T_{max}$  (153.2 °C) among thermograms OA factors (Fig. 1f3).  
339 However, the majority of organic molecules (e.g., C<sub>5</sub>H<sub>6</sub>O<sub>4</sub>, C<sub>4</sub>H<sub>6</sub>O<sub>5</sub>, C<sub>6</sub>H<sub>8</sub>O<sub>4</sub>, and C<sub>8</sub>H<sub>10</sub>O<sub>5</sub>) do not  
340 exhibit thermograms similar to that of Day-urban-ELVOA (Fig. S13). Instead, their thermograms  
341 demonstrate multimodal distributions and are contributed by multiple FIGAERO factors. For  
342 example, a mode of C<sub>5</sub>H<sub>6</sub>O<sub>4</sub> peaking in the LVOC range was mainly contributed by Day-urban-  
343 LVOA, while two modes peaking in the ELVOC range were primarily contributed by Day-aged-  
344 ELVOA and Day-urban-ELVOA, respectively. These results suggest that these molecules may  
345 originate from both direct desorption of organic aerosol and thermal decomposition of higher-  
346 molecular-weight compounds during heating. However, the majority of organic molecules in Day-  
347 urban-ELVOA did not show a similar thermogram to Day-urban-ELVOA (Fig. S10), which had a  
348 minor contribution to the thermogram peak located at ELVOC range. It indicates that this peak  
349 might be mainly contributed by decomposition products.

Formatted: Font colour: Auto

350

351 The biomass-burning related factor, biomass-burning less volatile organic aerosol (BB-LVOA,  
352 10% of FIGAERO-OA), had a low  $\overline{OS_c}$  (-0.07), the lowest O:C (0.74), and positive correlation with  
353 BBOA resolved from AMS ( $R=0.64$ , Fig. [S7S10b](#)). It presented a prominent peak at 19:00 LT and  
354 was identified by the distinctive tracer levoglucosan ( $C_6H_{10}O_5$ ), nitrocatechol ( $C_6H_5NO_4$ ), and  
355 nitrophenol ( $C_6H_5NO_3$ , Fig. 1) in the spectrum, which was frequently detected in biomass burning  
356 plumes (Gaston et al., 2016; Ye et al., 2021). In the upwind urban region of Heshan site, Ye et al.  
357 (2023) identified a biomass burning related factor in Guangzhou city using the FIGAERO-CIMS,  
358 with a distinct evening peak at 21:00 LT and more abundance oxygenated compounds (e.g.,  $C_7H_{10}O_5$   
359 and  $C_8H_{12}O_6$ ). The different oxidation level of BBOA between Guangzhou and Heshan, suggest the  
360 BB-LVOA in this study is more related to the direct BB emission, but the BB factor in Guangzhou  
361 is more resembled BB related SOA factor. This statement was supported by the fact that biomass  
362 burning activities were frequently observed near the measurement site during this study, while the  
363 biomass burning activities in urban areas was prohibited and can be transported from nearby  
364 suburban agricultural areas (Cai et al. 2023) .

365 The nighttime chemistry related less volatile OA (Night-OA, 15% of FIGAERO-OA) has the  
366 highest N:C (0.07) and exhibited an enhanced at nighttime (22:00-24:00 LT, Fig. 1). Notably, this  
367 nighttime factor was composed of a series of organic nitrates (e.g.,  $C_8H_{11}NO_7$ , and  $C_{10}H_{15}NO_7$ ),  
368 which was related to the products from monoterpenes oxidized by the  $NO_3$  radical or oxidation of  
369 biomass burning products during nighttime (Faxon et al., 2018; Decker et al., 2019). Noting that the  
370 levoglucosan ( $C_6H_{10}O_5$ ) was also abundant in the Night-LVOA, suggesting that part of this factor  
371 could be attributed to the nighttime aging process of biomass burning products (Jorga et al., 2021).  
372 The detailed discussion about the potential formation pathway of these six daytime FIGAERO-OA  
373 factors will be discussed in section 3.2.

374 The volatility of organic compounds was closely related to their chemical characteristics  
375 (Donahue et al., 2012). Figure 2 demonstrates the relationship between  $\log_{10} \overline{C^*}$  of thermogram  
376 factors and  $\overline{OS_c}$ , O:C, and number of carbons ( $nC$ ). In general, these factors exhibited a negative  
377 correlation ( $R=-0.60$  and  $-0.73$ ) with both the  $\overline{OS_c}$  and the O:C but showed a positive correlation  
378 ( $R=0.73$ ) with  $nC$  (Fig. 2), except for Day-urban-ELVOA. As aforementioned, the major component  
379 of Day-urban-ELVOA could be decomposition products of larger oxygenated molecules. Thus, the

380 chemical characteristic of Day-urban-ELVOA did not demonstrate a similar relationship of volatility  
381 versus molecule indicators (e.g., oxidation state, O:C and  $nC$ ) as other factors. The increase of  
382 carbon number usually lead to a decrease in volatility (Donahue et al., 2011), while this trend  
383 overturned in this campaign (Fig. 2c). Fig. 2d shows that  $\overline{OS}_c$  had a negative relationship ( $R=-0.84$ )  
384 with carbon number, suggesting that organic factors with a higher oxidation degree had a shorted  
385 carbon backbone. It could be partly owing to fragmentation of organic molecules during aging  
386 processes (Chacon-Madrid and Donahue, 2011; Jimenez et al., 2009). Consistently, two aged factors  
387 (Day-aged-LVOA and Day-aged-ELVOA) had a higher  $\overline{OS}_c$  and a lower carbon number than other  
388 factors. Additionally, it indicates that the increase in oxidation degree outweighed the effect of  
389 decreasing  $nC$ , leading to a reduction in the volatility of OA during this campaign.

390 The temporal variation of volatility distribution and mean  $C^*$  of FIGAERO-OA, the sum of  
391 six daytime factors in FIGAERO-OA and LOOA in AMS OA, mass fraction of eight FIGAERO-  
392 OA factors, and wind direction and speed are demonstrated in Fig. 3. As shown in Fig. 3, the  
393 increase of mean  $C^*$  during the daytime (6:00 LT to 18:00 LT, Fig. S14 a) is usually accompanied  
394 by the enhancement of daytime factors in FIGAERO-OA and LO-OOA from AMS (Fig. S14 b  
395 and c), indicating that the formation of these factors could notably increase OA volatility. Notably,  
396 FIGAERO-OA with a  $\log_{10} C^*$  of  $-1 \mu\text{g m}^{-3}$  showed pronounced enhancements during the  
397 increasing of mean  $C^*$ , implying that the volatility of six daytime factors might cluster around  $10^{-1}$   
398  $\mu\text{g m}^{-3}$  (Fig. S14 d). In Fig. 3b, distinct diurnal variation of  $\text{O}_x$  ( $\text{O}_x=\text{O}_3+\text{NO}_2$ ) was observed during  
399 the campaign. The maximum of  $\text{O}_x$  can be as high as  $230 \mu\text{g m}^{-3}$ , highlighting strong photochemical  
400 reaction. The daytime factors, especially Day- $\text{HNO}_x$ -LVOA (Fig. 3c), exhibited markable  
401 enhancements under weak northwesterly to northeasterly wind (Fig. 3d and Fig. S15). A  
402 backward trajectory analysis revealed that the measurement site was mainly affected by the urban  
403 pollutants from the city cluster around Guangzhou (Fig. S16). Two periods, which were long-  
404 range transport and urban air massed periods, respectively, were selected to further analyze the  
405 impact of urban pollutants on the formation and aging process of OA. The variation of OA volatility  
406 based on wind direction and speed, together with backward trajectory analysis, were also explored  
407 (Fig. S13 and Table S2). In general, during the urban air masses period, the site was influenced  
408 by regional urban plumes from the northeast city cluster, while the long-range transport period was

Formatted: Indent: First line: 2 ch

409 primarily associated with air masses advected from the northeast inland regions. More detailed  
410 discussion will be shown in the following section.

### 411 **3.2 Potential formation pathway of FIGAERO-OA**

412 Figure 4 demonstrates distinct differences in the diurnal variation of thermograms factors  
413 (including Day-HNO<sub>x</sub>-LVOA, Day-aged-LVOA, Day-urban-LVOA, and Day-urban-ELVOA)  
414 during long-range transport period and urban air masses period. During the urban air masses period,  
415 Day-HNO<sub>x</sub>-LVOA significantly increased from  $\sim 0.4 \mu\text{g m}^{-3}$  to  $\sim 4.8 \mu\text{g m}^{-3}$  in the daytime. The mass  
416 concentration of Day-urban-LVOA and Day-urban-ELVOA demonstrated daytime enhancements  
417 only during urban period, suggesting that the formation of these factors was closely related to the  
418 pollutants in the urban plumes. Consistently, During the urban air masses period, the maximum  
419 ozone concentration in the afternoon (12:00-18:00 LT,  $208.3 \mu\text{g m}^{-3}$ ) was higher than that ( $185.5 \mu\text{g m}^{-3}$ )  
420 during long-range transport period, indicating a stronger photochemical reaction in the urban  
421 plumes (Fig. 4). Thus, the daytime thermogram factors accounted for a higher fraction (79% vs 75%)  
422 of FIGAERO-OA (Fig. S14S17). Additionally, the average mass concentration of all thermogram  
423 factors ( $8.9 \pm 5.1 \mu\text{g m}^{-3}$ ) was noticeably increased compared to the long-range period ( $5.3 \pm 2.4 \mu\text{g m}^{-3}$ ).  
424 Elevated NO<sub>x</sub> concentration was observed in the urban plumes in the afternoon (12:00 LT-  
425 18:00 LT, 17.4 ppbv vs 11.7 ppbv), which might also affect the formation pathway of SOA. Both  
426 NO and NO/NO<sub>2</sub> remained at a relative low level (0.6-0.8 ppbv and <0.5) in the afternoon during  
427 these two periods (Fig. S15S18), suggesting an important role of low-NO-like pathway (Ye et al.,  
428 2023). Nihill et al. (2021) found that the production of OH and oxidized organic molecules would  
429 be suppressed under high NO/NO<sub>2</sub> (>1) condition. Notably, Day-HNO<sub>x</sub>-LVOA accounted for the  
430 largest portion (29%) of FIGAERO-OA in the afternoon (12:00-18:00 LT, Fig. S16S19), followed  
431 by Day-aged-LVOA (21%), while Day-LNO<sub>x</sub>-LVOA contributed only 6%. In contrast, during the  
432 long-range transport period, the mass fraction of Day-LNO<sub>x</sub>-LVOA significantly increased (from  
433 6% to 15%) along with a decrease in Day-HNO<sub>x</sub>-LVOA (from 29% to 21%). These results indicate  
434 that elevated NO<sub>x</sub> concentration in urban plumes might alter the formation pathway of SOA (Cai et  
435 al., 2024). Note that the sum of six daytime FIGAERO factors showed a positive relationship  
436 (R=0.80 and 0.76, respectively) with LOOA during both periods (Fig. S20). However, the slope  
437 (0.81) of the linear regression during the urban air masses period was higher than that (0.58) during  
438 the long-range transport period, indicating that a higher fraction of LOOA could be detected by the

439 FIGAERO-CIMS during urban air masses period. This difference could be related to the  
440 discrepancy in OA volatility. According to Cai et al. (2024), the volatility of OA was higher during  
441 the urban air masses period. Note that the sum of six daytime FIGAERO factors showed a positive  
442 relationship ( $R=0.80$  and  $0.76$ , respectively) with LOOA during both periods (Fig. S20). However,  
443 the slope ( $0.81$ ) of the linear regression during the urban air masses period was higher than that  
444 ( $0.58$ ) during the long range transport period, indicating that a higher fraction of LOOA could be  
445 detected by the FIGAERO-CIMS during urban air masses period. This difference could be related  
446 to the discrepancy in OA volatility. According to Cai et al. (2024), the volatility of OA was higher  
447 during the urban air masses period.

448 To explore the potential formation pathway of daytime factors, figure 5 demonstrates the  
449 variation of mass concentrations of six daytime factors as a function of  $O_x$ , total gas-phase organic  
450 molecules measured by the FIGAERO-CIMS (referred as organic vapors), and  $NO_3^-/SIA$ . Five  
451 factors, excluding Day-urban-LVOA, exhibited positive correlations with  $O_x$ , highlighting the  
452 critical role of photochemical reactions in their formation. Previous studies have demonstrated that  
453 gas–particle partitioning plays a key role in SOA formation (Nie et al., 2022; Wang et al., 2022). In  
454 this study, organic vapors had strong positive correlations with Day- $HNO_x$ -LVOA ( $R=0.73$ ) and  
455 Day- $LNO_x$ -LVOA ( $R=0.74$ ), suggesting that these factors were mainly formed via gas-particle  
456 partitioning. The median concentration of Day- $HNO_x$ -LVOA dramatically increased (from  $\sim 0$  to  
457  $\sim 5.6 \mu\text{g m}^{-3}$ ) with rising organic vapors, whereas a comparable enhancement was not observed for  
458 Day- $LNO_x$ -LVOA (Fig. 5 b1 and b2).

459 Furthermore,  $NO_x$  impact on Day- $HNO_x$ -LVOA and Day- $HNO_x$ -LVOA was investigated here.  
460 Fig. S17S21 show Day- $HNO_x$ -LVOA concentrations were consistently higher under elevated  $NO_x$   
461 conditions, while Day- $HNO_x$ -LVOA decreased with increasing  $NO_x$  level. Figure 6a displays the  
462 mass ratio of Day- $HNO_x$ -LVOA to Day- $LNO_x$ -LVOA obviously increased with organic vapors (up  
463 to  $12\sim26$ ) under high  $NO_x$  condition ( $>20$  ppbv), while the ratio remained at approximately 2 at  
464 low  $NO_x$  level ( $<10$  ppbv). These overall results suggest that Day- $HNO_x$ -LVOA formation was  
465 predominantly governed by gas-particle partitioning under high  $NO_x$  condition, which were  
466 typically sustained during urban air masses period (Fig. 2d). Figure 6b compares the relative mass  
467 fraction of molecular composition in two gas-particle partitioning related factors, Day- $HNO_x$ -  
468 LVOA and Day- $LNO_x$ -LVOA. The mass fraction of species was derived from the signal profile of

Formatted: Font: Italic, Subscript

469 corresponding factors based on their sensitivity (Ye et al., 2021). Day-HNO<sub>x</sub>-LVOA presented  
470 greater proportions ( $10^{-5} \sim 10^{-3}$ ) of organic nitrates (ONs) than Day-LNO<sub>x</sub>-LVOA ( $10^{-11} \sim 10^{-9}$ ),  
471 including C<sub>4</sub>H<sub>7</sub>NO<sub>6</sub>, C<sub>8</sub>H<sub>9</sub>NO<sub>4</sub>, C<sub>8</sub>H<sub>11</sub>NO<sub>7</sub>, as well as nitrophenols (e.g., C<sub>7</sub>H<sub>7</sub>NO<sub>3</sub>), which are  
472 characterized by relatively low  $\overline{OS_c}$ . These compounds were probably attributed to the SOA  
473 formation under elevated NO<sub>x</sub> concentration (Fig. 2d). In contrast, Day-LNO<sub>x</sub>-LVOA was enriched  
474 in non-nitrogen-containing species (e.g., C<sub>4</sub>H<sub>6</sub>O<sub>3</sub>, C<sub>5</sub>H<sub>10</sub>O<sub>3</sub>, C<sub>11</sub>H<sub>17</sub>O<sub>6</sub>), which exhibited a higher  
475  $\overline{OS_c}$ . These results indicate that NO<sub>x</sub> exerts contrasting effects on the formation of these two gas-  
476 particle partitioning-related factors.

477 Previous studies show that NO<sub>x</sub> has a nonlinear effect on the formation of highly oxygenated  
478 organic (HOM) compounds by influencing the atmospheric oxidation capacity and RO<sub>2</sub>  
479 autoxidation (Xu et al., 2025; Pye et al., 2019; Shrivastava et al., 2019). NO<sub>x</sub> could suppress the  
480 production of low-volatility molecules by inhibiting autoxidation (Rissanen, 2018; Praske et al.,  
481 2018), while Nie et al. (2023) found that NO could enhance the formation of HOM at low NO  
482 condition (< 82 pptv). During this campaign, the average NO<sub>x</sub> and NO was about 24.0 ppbv and 2.3  
483 ppbv, respectively, substantially higher than the “low-NO-regime” described by Nie et al. (2023).  
484 Our previous study reported a lower concentration of organic vapors with a high  $\overline{OS_c}$  within urban  
485 plumes during the same campaign (Cai et al., 2024). We investigate diurnal evolution of organic  
486 compositions under long-range transport and urban air masses periods (Fig. S22). Mass  
487 concentrations of CHON increase during the daytime in both periods, with a more pronounced  
488 enhancement observed in urban air masses (Fig. S22a). However, the mass fraction of CHON was  
489 lower during the urban air masses period than during the long-range transport period. We speculated  
490 that elevated NO<sub>x</sub> enhances overall oxidation and product formation rather than selectively  
491 enriching nitrogen-containing compounds. This interpretation is consistent with results from our  
492 previous observation-constrained box-model simulations, in which production rates of OH and  
493 organic peroxy radicals (RO<sub>2</sub>) were evaluated under varying NO<sub>x</sub> and VOC conditions (Cai et al.,  
494 2024). The modeled P(OH) were close to the transition regime, indicating that elevated NO<sub>x</sub> can  
495 enhance atmospheric oxidation capacity. In contrast, the P(RO<sub>2</sub>) was in the VOC-limited regime  
496 and decreased with increasing NO<sub>x</sub>. Consistent with these results, Fig. S22c shows that the mass  
497 fraction of highly oxygenated organic molecules (O ≥ 6) is lower during urban air masses period.  
498 Concurrently, species with low oxygen numbers (O ≤ 3) become relatively more abundant in the

Formatted: Font colour: Auto

499 [urban plumes \(Fig. S22c\)](#), indicating a shift in the oxidation product distribution toward less  
500 [oxygenated and potentially more volatile compounds](#), the  $\text{NO}_x$ -driven suppression of  
501 [multigenerational autoxidation inferred from the box-model results](#). This suppression of oxidation  
502 [is observed for both CHON and CHO species](#). The average O:C of CHON (Fig. S22b) and CHO  
503 (Fig. S22e) are both lower during the urban air masses period, suggesting that enhanced  $\text{NO}_x$  broadly  
504 [suppresses autoxidation across organic compound classes](#).

505 Furthermore, as illustrated in Fig. S18S23, the mass concentration of SVOC ( $-0.5 < \log_{10} C^* <$   
506  $2.5 \mu\text{g m}^{-3}$ ) and LVOC ( $-3.5 < \log_{10} C^* < -0.5 \mu\text{g m}^{-3}$ , Donahue et al., 2012) in the gas phase exhibited  
507 an increase ( $2.5 \mu\text{g m}^{-3}$  at  $\text{NO}_x < 10 \text{ ppbv}$  vs  $3.3 \mu\text{g m}^{-3}$  at  $\text{NO}_x \geq 30 \text{ ppbv}$ ) with the increase in  $\text{NO}_x$ ,  
508 suggesting that these species likely contributed to the formation of Day-HNO<sub>x</sub>-LVOA. [Xu et al.](#)  
509 (2014) found that both SOA volatility and oxidation state exhibited a nonlinear response to  $\text{NO}_x$  in  
510 [a series of chamber environment](#). SOA volatility decreases with increasing  $\text{NO}_x$  level when the ratio  
511 [of initial NO to isoprene was lower than 3](#). At higher  $\text{NO}_x$  level, higher volatile SOA was produced,  
512 [probably owing to the more competitive  \$\text{RO}\_2 + \text{NO}\$  pathway](#). Figure 5 c1 and c2 investigate the  
513 relationship between these two factors and  $\text{NO}_3^-/\text{SIA}$ . Day-HNO<sub>x</sub>-LVOA had a weak correlation  
514 ( $R=0.30$ ) with  $\text{NO}_3^-/\text{SIA}$ , while this trend overturned ( $R=-0.35$ ) for Day-LNO<sub>x</sub>-LVOA. Yang et al.  
515 (2022) showed that  $\text{OH} + \text{NO}_2$  pathway mainly contribute to the formation of nitrate in this campaign.  
516 Together, these results indicate that elevated  $\text{NO}_x$  suppressed the formation of highly oxygenated  
517 organic compounds, thereby limiting the contribution to Day-LNO<sub>x</sub>-LVOA. Thus, the Day-LNO<sub>x</sub>-  
518 LVOA was more likely formed via gas-particle partitioning under relatively low  $\text{NO}_x$  condition.

519 It is worth noting that C<sub>4</sub>H<sub>7</sub>NO<sub>5</sub>, likely originating from isoprene photooxidation in the  
520 presence of  $\text{NO}_x$  (Fisher et al., 2016; Paulot et al., 2009), also show a higher fraction in Day-LNO<sub>x</sub>-  
521 LVOA ( $9.36 \times 10^{-5}$  vs  $4.93 \times 10^{-11}$  in Day-HNO<sub>x</sub>-LVOA). A plausible explanation is that Heshan site,  
522 located at a suburban region, experienced ambient  $\text{NO}_x$  levels ( $\sim 13 \text{ ppb}$  in the afternoon) sufficient  
523 to facilitate the formation of C<sub>4</sub>H<sub>7</sub>NO<sub>5</sub>. It is further supported by the observation that both particle-  
524 and gas-phase C<sub>4</sub>H<sub>7</sub>NO<sub>5</sub> showed no significant variation with increasing  $\text{NO}_x$  (Fig. S1924).

525 For the two urban-related factors, a positive correlation with  $\text{O}_x$  was observed only during the  
526 urban air masses period ( $R=0.46$  and  $0.64$  vs  $-0.05$  and  $0.28$  in the long-range transport period, Fig.  
527 S1920 a and c). Notably, Day-urban-LVOA increased from  $\sim 1.0$  to  $\sim 2.6 \mu\text{g m}^{-3}$  as  $\text{O}_x$  rose from  $75$   
528 to  $275 \mu\text{g m}^{-3}$  during this period, while it remained relatively stable ( $\sim 0.4 \mu\text{g m}^{-3}$ ) during the long-

529 range transport period (Fig. S20-S25). In addition, Day-urban-LVOA showed only a limited  
530 similarity in its variation trend to Day-HNO<sub>x</sub>-LVOA during the urban air mass period (Fig. S26).  
531 This finding supports the hypothesis that the daytime formation of urban-related OA factors was  
532 closely related to the urban pollutants. Additionally, Day-urban-ELVOA exhibited a positive  
533 correlation with organic vapors ( $R = 0.65$ , Fig. S20b-S25b), while such a correlation was not  
534 observed for Day-urban-LVOA. It implies that Day-urban-ELVOA may primarily form through  
535 gas-particle partitioning during the urban air mass period.

536 Day-urban-LVOA was also positively correlated with NO<sub>3</sub><sup>-</sup>/SIA (Fig. 5c), consistent with the  
537 concurrent enhancement of nitrate and SOA during haze episodes (Ye et al., 2023; Zheng et al.,  
538 2021). During the urban air masses period, nitrate demonstrates a bimodal diurnal variation with  
539 peaks in both the morning and afternoon (Fig. S24-S27), the latter peak likely attributed to OH+NO<sub>2</sub>  
540 pathway (Yang et al., 2022). Day-urban-LVOA had a significant correlation ( $R=0.97$ ) with  
541 succinic acid (C<sub>4</sub>H<sub>6</sub>O<sub>4</sub>) in the particle phase (Fig. S22-S28), which was previously reported to form  
542 via multiphase reaction during haze episode in megacity (Zhao et al., 2018; Zheng et al., 2021). As  
543 shown in Fig. S23-S29, Day-urban-LVOA also increased with the ratio of the aerosol liquid water  
544 content (ALWC) to PM<sub>1</sub>, further indicating that aqueous processes in urban plumes played an  
545 important role in its enhancement.

546 For the aging factors, Day-aged-LVOA and Day-aged-ELVOA exhibited peak concentrations  
547 about 3 hours later (at about 18:00 LT, Fig. 4) than other day factors (15:00 LT). It suggests that the  
548 two aged factors might originate from the photochemical aging processes of preexisting organic  
549 aerosols. To further explore the formation and aging process of these daytime factors, we estimated  
550 their daytime enhancement ( $\Delta$ ). For factors peaked at 15:00 LT, the  $\Delta$  was estimated as the difference  
551 between the average mass concentration during 00:00-6:00 LT and 12:00-18:00 LT. For factors  
552 peaking at about 18:00 LT,  $\Delta$  was regarded as the difference between the average mass  
553 concentration during 6:00-12:00 LT and 15:00-21:00 LT, since these factors remained at a relatively  
554 high-level during nighttime probably owing to lower boundary layer height. The  $\Delta$  Day-aged-  
555 LVOA showed strong positive correlations with  $\Delta$  Day-HNO<sub>x</sub>-LVOA ( $R=0.73$ ),  $\Delta$  Day-urban-  
556 LVOA ( $R=0.77$ ), and  $\Delta$  Day-LNO<sub>x</sub>-LVOA ( $R=0.64$ , Fig. 7a), suggesting that its formation might  
557 be closely associated with the aging processes of these three factors. Similarly,  $\Delta$  Day-aged-ELVOA  
558 was positively correlated with both  $\Delta$  Day-LNO<sub>x</sub>-LVOA ( $R=0.61$ ),  $\Delta$  Day-urban-LVOA ( $R=0.67$ ),

559 and  $\Delta$  Day-urban-ELVOA ( $R=0.73$ , Fig. 7c). In contrast, we did not observe such correlations  
560 between  $\Delta$  Day-aged-ELVOA and  $\Delta$  Day-HNO<sub>x</sub>-LVOA ( $R=0.49$ , Fig. 7c). It implies that the  
561 formation of Day-aged-ELVOA was likely more influenced by the aging of urban-related factors  
562 and Day-LNO<sub>x</sub>-LVOA.

### 563 3.3 Comparison with AMS OA

564 Adopting PMF analysis to thermogram datasets provides valuable insights into the formation  
565 and aging processes of SOA. However, the representativeness of FIGAERO-OA still requires  
566 evaluation. Figure 8 compares FIGAERO-OA with AMS-OA during two different periods. In  
567 general, FIGAERO-OA could not explain MO-OOA and HOA identified in AMS OA, given that  
568 all thermogram factors had a weak correlation ( $R=-0.18$ – $0.36$ ) between these two factors (Table S2).  
569 MO-OOA, which had the highest O:C (1.0) among all AMS factors (0.32–1.0) (Cai et al., 2024),  
570 was likely low volatile, meaning that much of this fraction might not have been vaporized during  
571 the heating process. [Xu et al. \(2019\) investigate the volatility of different OA factors using the TD+AMS method and found that MO-OOA evaporated ~52% at T=175°C. Another TD+AMS field study in the North China Plain suggested that the volatility of MO-OOA varied with RH levels, more MO-OOA evaporate at higher RH levels \(RH>70, Xu et al., 2021\), suggesting that MO-OOA compounds formed at high RH condition could be higher volatile. During this campaign, the RH varied from 25% to 92% which likely caused variability in MO-OOA volatility and thus in the fraction desorbed at 175 °C. This variability might explain the low correlation between MO-OOA in AMS and all FIGAERO-OA factors.](#) HOA mainly consists of hydrocarbon-like organic  
572 compounds, which could not be detected by the FIGAERO-CIMS. The iodide source of the  
573 FIGAREO-CIMS is selective towards multi-functional organic compounds (Lee et al., 2014),  
574 making it less sensitive to detection hydrocarbon-like species. Ye et al. (2023) preformed  
575 factorization analysis of data obtained from the FIGAERO-CIMS and AMS and suggested that  
576 FIGAERGAERO-CIMS and AMS and suggested that FIGAERO-derived OA factors could not  
577 account for all primary OA components resolved by AMS, including COA, NOA, and HOA. These  
578 findings highlight the need for further investigations into the chemical characteristics of primary  
579 OA to better understand their emission signatures and atmospheric evolution.

580 BBSOA in AMS-OA had a bimodal diurnal distribution with an afternoon peak (~ 14:00 LT)  
581 and an evening peak (~ 17:00 LT, Fig. [S24S30](#)). The enhancement was more pronounced in the

589 afternoon ( $\sim 1.6$  to  $\sim 3.6 \mu\text{g m}^{-3}$ ) compared to the evening ( $\sim 2.9$  to  $\sim 4.0 \mu\text{g m}^{-3}$ ). Thus, we classify  
590 both BBSOA and LOOA as daytime SOA. Six thermogram daytime factors could explain the  
591 majority (82% on average) of daytime SOA with the explained fraction increasing from 78% during  
592 the long-range transport period to 85% during the urban air masses period (Fig. 8 a and b). In both  
593 periods, the summed thermogram daytime factors exhibited a diurnal variation like that of  
594 LOOA+BBSOA (Fig. 8 c and d). Thermogram daytime OA was close to AMS daytime OA in the  
595 morning but fell below AMS OA afternoon. The discrepancy in the afternoon could be related to  
596 the decrease in OA volatility through strong photochemical reactions. Since the heating temperature  
597 of the FIGAERO-CIMS was set at  $175^\circ\text{C}$ , compounds of very low volatility might not have been  
598 fully detected. This discrepancy narrowed during the urban air masses, likely owing to the strong  
599 SOA formation through gas-particle partitioning, which increased OA volatility (Cai et al., 2024).  
600 The gap persisted overnight, owing to suppressed vertical mixing under lower boundary layer  
601 conditions.

602 FIGAERO-OA explained about 13% of BBOA in AMS OA during the campaign and this ratio  
603 remained relatively stable across different periods compared with daytime SOA (Fig. 8 a and b).  
604 Because BBOA is closely tied to local biomass burning activities, air mass variations likely had  
605 only a minor influence on its chemical characteristics. BB-LVOA showed a diurnal pattern similar  
606 to both BBOA in AMS-OA and levoglucosan (Fig. 9a), with an evening peak around 18:30 LT,  
607 confirming their close association with biomass burning emissions. For nighttime chemistry related  
608 factor, both Night-OA (from AMS) and Night-LVOA (from thermograms) increase during the  
609 nighttime, while they did not share a similar diurnal pattern (Fig. 9b). Night-LVOA peaked at about  
610 20:00 LT and decreased after 4:00 LT, while Night-OA peaked later, at about 06:00 LT, and declined  
611 in the morning. It suggested that Night-LVOA identified by FIGAERO-CIMS might not be able to  
612 fully capture the evolution of organic compounds involved in nighttime chemistry, which can  
613 explain 48% of Night-OA in AMS-OA. Given that the majority of organic compounds formed  
614 through the nighttime chemistry were oxygenated and could be detected by FIGAERO CIMS (Wu  
615 et al., 2021), we speculated that the volatility of organic compounds decreased overnight, resulting  
616 that some low volatility organic aerosols would not be fully vaporized during the heating process.

617 [Xu et al. \(2019\) found that nighttime MO-OOA exhibited lower volatility compared with daytime  
618 MO-OOA, likely due to differences in precursors, formation mechanisms, and meteorological](#)

619 conditions. Moreover, organic nitrates generally have lower volatility than hydroxylated species  
620 with the same carbon number (Donahue et al., 2011; Ren et al., 2022). It suggested that a higher  
621 fraction of nighttime organic nitrates could lead to lower OA volatility (Kiendler-Scharr et al., 2016).

Formatted: Font colour: Auto

## 622 4. Conclusion

623 In this study, we applied a PMF analysis to field thermogram data set measured by the  
624 FIGAERO-CIMS and classified the factors based on their potential formation pathways and  
625 volatility. Based on the PMF analysis to thermograms data sets, six daytime OA factors, a biomass  
626 burning related factor, and nighttime chemistry related factor were identified. The formation of Day-  
627  $\text{HNO}_x$ -LVOA and Day- $\text{LNO}_x$ -LVOA was closely related to gas-particle partitioning, while Day-  
628  $\text{HNO}_x$ -LVOA was observed to be formed with organic vapors under high  $\text{NO}_x$  condition. The  
629 increase in  $\text{NO}_x$  concentration might inhibit the production of highly oxygenated compounds (Cai  
630 et al., 2024), which could explain the relatively high volatility of Day- $\text{HNO}_x$ -LVOA. Two urban  
631 related factors, Day-urban-LVOA and Day-urban-ELVOA, were identified, which only showed a  
632 daytime enhancement in urban plumes. The former might originate from aqueous processes, while  
633 the latter was likely formed through gas-particle partitioning. Our results demonstrated that  
634 photochemical-derived gas-particle partitioning mainly contributed to OA formation in downwind  
635 urban plumes.

636 Daytime aging processes of organic aerosol were observed and leading to the decrease in  
637 volatility with two aged factors (Day-aged-LVOA and Day-aged-ELVOA) identified. The formation  
638 of Day-aged-LVOA was related to the photochemical aging processes of Day- $\text{HNO}_x$ -LVOA, Day-  
639  $\text{LNO}_x$ -LVOA, Day-urban-LVOA, and Day-urban-ELVOA, while Day-aged-ELVOA originates  
640 from the aging processes of Day- $\text{LNO}_x$ -LVOA, Day-urban-LVOA, and Day-urban-ELVOA. In  
641 general, these six thermogram daytime factors could explain the majority of daytime SOA in AMS  
642 OA, and this ratio increase from 79% during the long-range transport period to 85% during the  
643 urban air masses period, probably owing to a higher OA volatility (Cai et al., 2024). While  
644 FIGAERO-OA is unable to explain hydrocarbon like OA (HOA) and more oxygenated OA (MOOA),  
645 since the FIGAERO-CIMS could not detect hydrocarbon molecules and low volatility organic  
646 compounds with a volatilization temperature higher than 170 °C. For biomass-related OA, BB-  
647 LVOA could explain about 11%-13% of the BBOA in AMS OA, sharing a similar diurnal pattern,

648 indicating that adopting a PMF analysis to thermogram profile could capture biomass burning events.  
649 While Night-LVOA had a different diurnal pattern with Night-OA in AMS OA, implying that this  
650 thermogram factor was not unable to represent the evolution of OA during the nighttime.

651 To our knowledge, existing field studies applying PMF to FIGAERO-CIMS data have  
652 primarily focused on the mass concentrations or signal intensities of organic compounds rather than  
653 their thermograms. Chen et al. (2020) applied PMF to FIGAERO-CIMS datasets collected in  
654 Yorkville, GA, and reported substantial contributions of isoprene- and monoterpene-derived SOA  
655 during both daytime and nighttime. Using the same approach, Ye et al. (2023) showed that low-NO-  
656 like oxidation pathways played a significant role in SOA formation in urban environments. However,  
657 these PMF analyses did not provide volatility information, which limits our ability to fully  
658 understand the formation mechanisms and aging processes of OA. Lee et al. (2020) demonstrated  
659 that combining molecular-level composition measurements with volatility information enables the  
660 resolution of organic aerosol formation and aging pathways in the atmosphere, providing direct  
661 constraints on how oxidation processes alter both chemical functionality and volatility during  
662 aerosol evolution. Buchholz et al. (2020) performed PMF analysis on FIGAERO-CIMS  
663 thermogram datasets in laboratory experiments and demonstrated that both OA volatility and  
664 composition varied with relative humidity. Nevertheless, applications of thermogram-based PMF to  
665 ambient field measurements remain scarce.

666 Our results show that applying PMF directly to thermogram profiles from field observations  
667 yields additional and valuable volatility information that is not accessible from traditional mass- or  
668 signal-based PMF analyses. This added dimension is particularly useful for OA source  
669 apportionment. Our results reveal that applying a PMF analysis to thermogram profiles in field  
670 campaign could provide additional volatility information, which will benefit in OA source  
671 apportionment. Along with PMF analysis of AMS or ACSM data, it can provide crucial information  
672 in understanding the formation and aging processes of OA. Using this method, we found that the  
673 daytime atmospheric evolution of SOA involved gas-particle partitioning, aqueous-phase reactions,  
674 and photochemical aging, highlighting the complexity of daytime SOA formation. Moreover, SOA  
675 volatility was strongly dependent on its formation pathways. variations in NO<sub>x</sub> not only influenced  
676 atmospheric oxidation but also modified SOA volatility by altering formation mechanisms.

677 Nevertheless, further investigations are required to clarify the role of urban plumes in shaping SOA  
678 formation and its physicochemical properties.

679

680

681 *Data availability.* Data from the measurements are available at 10.6084/m9.figshare.30155584

682

683 *Supplement.* The supplement related to this article is available online at xxx.

684

685 *Author contributions.* M.C., W. H., and B.Y. designed the research. M.C., B.Y., W.H., Y.C., S. H.,  
686 S.Y., W.C., Y. P., and J.Z. performed the measurements. M. C., B.Y., W.H., Y.C., S. H., Z. D., and  
687 D. C. analyzed the data. M. C., W.H. and B.Y. wrote the paper with contributions from all co-authors.

688

689 *Competing interests.* The authors declare that they have no conflict of interest.

690

691 *Financial support.* This work was supported by Guangdong Basic and Applied Basic Research  
692 Foundation (grant nos. 2024A1515030221, 2023A1515012240), National Natural Science  
693 Foundation of China (grant no. 42305123, 42375105), Science and Technology Projects in  
694 Guangzhou (grant no. 2025A04J4493), the Key Innovation Team of Guangdong Meteorological  
695 Bureau (No. GRMCTD202506-ZD06) , and Central Public interest Scientific Institution Basal  
696 Research Fund of South China Institute of Environmental Sciences, MEE (grant no. PM-zx097-  
697 202506-214).

698

699 **Reference**

700 Al-Naiema, I. M., Hettiyadura, A. P. S., Wallace, H. W., Sanchez, N. P., Madler, C. J., Cevik, B. K.,  
701 Bui, A. A. T., Kettler, J., Griffin, R. J., and Stone, E. A.: Source apportionment of fine particulate matter  
702 in Houston, Texas: insights to secondary organic aerosols, *Atmos. Chem. Phys.*, 18, 15601-15622,  
703 10.5194/acp-18-15601-2018, 2018.

704 Apt, J. S., Brauer, M., Cohen, A. J., Ezzati, M., and Pope, C. A., III: Ambient PM<sub>2.5</sub> Reduces  
705 Global and Regional Life Expectancy, *Environmental Science & Technology Letters*, 5, 546-551,  
706 10.1021/acs.estlett.8b00360, 2018.

707 Arias, P. A., Bellouin, N., Coppola, E., Jones, R. G., Krinner, G., Marotzke, J., Naik, V., Palmer, M.  
708 D., Plattner, G. K., Rogelj, J., Rojas, M., Sillmann, J., Storelvmo, T., Thorne, P. W., Trewin, B., Achuta  
709 Rao, K., Adhikary, B., Allan, R. P., Armour, K., Bala, G., Barimalala, R., Berger, S., Canadell, J. G.,  
710 Cassou, C., Cherchi, A., Collins, W., Collins, W. D., Connors, S. L., Corti, S., Cruz, F., Dentener, F. J.,  
711 Dereczynski, C., Di Luca, A., Diongue Niang, A., Doblas-Reyes, F. J., Dosio, A., Douville, H.,  
712 Engelbrecht, F., Eyring, V., Fischer, E., Forster, P., Fox-Kemper, B., Fuglestvedt, J. S., Fyfe, J. C., Gillett,  
713 N. P., Goldfarb, L., Gorodetskaya, I., Gutierrez, J. M., Hamdi, R., Hawkins, E., Hewitt, H. T., Hope, P.,  
714 Islam, A. S., Jones, C., Kaufman, D. S., Kopp, R. E., Kosaka, Y., Kossin, J., Krakovska, S., Lee, J. Y., Li,  
715 J., Mauritsen, T., Maycock, T. K., Meinshausen, M., Min, S. K., Monteiro, P. M. S., Ngo-Duc, T., Otto,  
716 F., Pinto, I., Pirani, A., Raghavan, K., Ranasinghe, R., Ruane, A. C., Ruiz, L., Sallée, J. B., Samset, B.  
717 H., Sathyendranath, S., Seneviratne, S. I., Sörensson, A. A., Szopa, S., Takayabu, I., Tréguier, A. M., van  
718 den Hurk, B., Vautard, R., von Schuckmann, K., Zaehle, S., Zhang, X., and Zickfeld, K.: Technical  
719 Summary, in: *Climate Change 2021: The Physical Science Basis. Contribution of Working Group I to*  
720 *the Sixth Assessment Report of the Intergovernmental Panel on Climate Change*, edited by: Masson-  
721 Delmotte, V., Zhai, P., Pirani, A., Connors, S. L., Péan, C., Berger, S., Caud, N., Chen, Y., Goldfarb, L.,  
722 Gomis, M. I., Huang, M., Leitzell, K., Lonnoy, E., Matthews, J. B. R., Maycock, T. K., Waterfield, T.,  
723 Yelekçi, O., Yu, R., and Zhou, B., Cambridge University Press, Cambridge, United Kingdom and New  
724 York, NY, USA, 33–144, 10.1017/9781009157896.002, 2021.

725 Barsanti, K. C. and Pankow, J. F.: Thermodynamics of the formation of atmospheric organic  
726 particulate matter by accretion reactions—Part 1: aldehydes and ketones, *Atmospheric Environment*, 38,  
727 4371-4382, <https://doi.org/10.1016/j.atmosenv.2004.03.035>, 2004.

728 Buchholz, A., Ylisirniö, A., Huang, W., Mohr, C., Canagaratna, M., Worsnop, D. R., Schobesberger,  
729 S., and Virtanen, A.: Deconvolution of FIGAERO–CIMS thermal desorption profiles using positive  
730 matrix factorisation to identify chemical and physical processes during particle evaporation, *Atmos.  
731 Chem. Phys.*, 20, 7693-7716, 10.5194/acp-20-7693-2020, 2020.

732 Cai, M., Ye, C., Yuan, B., Huang, S., Zheng, E., Yang, S., Wang, Z., Lin, Y., Li, T., Hu, W., Chen,  
733 W., Song, Q., Li, W., Peng, Y., Liang, B., Sun, Q., Zhao, J., Chen, D., Sun, J., Yang, Z., and Shao, M.:  
734 Enhanced daytime secondary aerosol formation driven by gas–particle partitioning in downwind urban  
735 plumes, *Atmos. Chem. Phys.*, 24, 13065-13079, 10.5194/acp-24-13065-2024, 2024.

736 Cai, Y., Ye, C., Chen, W., Hu, W., Song, W., Peng, Y., Huang, S., Qi, J., Wang, S., Wang, C., Wu, C.,  
737 Wang, Z., Wang, B., Huang, X., He, L., Gligorovski, S., Yuan, B., Shao, M., and Wang, X.: The important  
738 contribution of secondary formation and biomass burning to oxidized organic nitrogen (OON) in a  
739 polluted urban area: insights from in situ measurements of a chemical ionization mass spectrometer  
740 (CIMS), *Atmos. Chem. Phys.*, 23, 8855-8877, 10.5194/acp-23-8855-2023, 2023.

741 Chacon-Madrid, H. J. and Donahue, N. M.: Fragmentation vs. functionalization: chemical aging

742 and organic aerosol formation, *Atmos. Chem. Phys.*, 11, 10553-10563, 10.5194/acp-11-10553-2011,  
743 2011.

744 Charan, S. M., Huang, Y., and Seinfeld, J. H.: Computational Simulation of Secondary Organic  
745 Aerosol Formation in Laboratory Chambers, *Chemical Reviews*, 119, 11912-11944,  
746 10.1021/acs.chemrev.9b00358, 2019.

747 Canonaco, F., Crippa, M., Slowik, J. G., Baltensperger, U., and Prévôt, A. S. H.: SoFi, an IGOR-  
748 based interface for the efficient use of the generalized multilinear engine (ME-2) for the source  
749 apportionment: ME-2 application to aerosol mass spectrometer data, *Atmos. Meas. Tech.*, 6, 3649-3661,  
750 10.5194/amt-6-3649-2013, 2013.

751 Chen, G., Sosedova, Y., Canonaco, F., Fröhlich, R., Tobler, A., Vlachou, A., Daellenbach, K. R.,  
752 Bozzetti, C., Hueglin, C., Graf, P., Baltensperger, U., Slowik, J. G., El Haddad, I., and Prévôt, A. S. H.:  
753 Time-dependent source apportionment of submicron organic aerosol for a rural site in an alpine valley  
754 using a rolling positive matrix factorisation (PMF) window, *Atmos. Chem. Phys.*, 21, 15081-15101,  
755 10.5194/acp-21-15081-2021, 2021a.

756 Chen, W. T., Shao, M., Lu, S. H., Wang, M., Zeng, L. M., Yuan, B., and Liu, Y.: Understanding  
757 primary and secondary sources of ambient carbonyl compounds in Beijing using the PMF model, *Atmos.*  
758 *Chem. Phys.*, 14, 3047-3062, 10.5194/acp-14-3047-2014, 2014.

759 Chen, W., Hu, W., Tao, Z., Cai, Y., Cai, M., Zhu, M., Ye, Y., Zhou, H., Jiang, H., Li, J., Song, W.,  
760 Zhou, J., Huang, S., Yuan, B., Shao, M., Feng, Q., Li, Y., Isaacman-VanWertz, G., Stark, H., Day, D. A.,  
761 Campuzano-Jost, P., Jimenez, J. L., and Wang, X.: Quantitative Characterization of the Volatility  
762 Distribution of Organic Aerosols in a Polluted Urban Area: Intercomparison Between Thermoenunder  
763 and Molecular Measurements, *Journal of Geophysical Research: Atmospheres*, 129, e2023JD040284,  
764 <https://doi.org/10.1029/2023JD040284>, 2024.

765 Chen, Y., Guo, H., Nah, T., Tanner, D. J., Sullivan, A. P., Takeuchi, M., Gao, Z., Vasilakos, P., Russell,  
766 A. G., Baumann, K., Huey, L. G., Weber, R. J., and Ng, N. L.: Low-Molecular-Weight Carboxylic Acids  
767 in the Southeastern U.S.: Formation, Partitioning, and Implications for Organic Aerosol Aging,  
768 *Environmental Science & Technology*, 55, 6688-6699, 10.1021/acs.est.1c01413, 2021b.

769 Chen, Y., Takeuchi, M., Nah, T., Xu, L., Canagaratna, M. R., Stark, H., Baumann, K., Canonaco, F.,  
770 Prévôt, A. S. H., Huey, L. G., Weber, R. J., and Ng, N. L.: Chemical characterization of secondary organic  
771 aerosol at a rural site in the southeastern US: insights from simultaneous high-resolution time-of-flight  
772 aerosol mass spectrometer (HR-ToF-AMS) and FIGAERO chemical ionization mass spectrometer  
773 (CIMS) measurements, *Atmos. Chem. Phys.*, 20, 8421-8440, 10.5194/acp-20-8421-2020, 2020.

774 Decker, Z. C. J., Zarzana, K. J., Coggon, M., Min, K.-E., Pollack, I., Ryerson, T. B., Peischl, J.,  
775 Edwards, P., Dubé, W. P., Markovic, M. Z., Roberts, J. M., Veres, P. R., Graus, M., Warneke, C., de Gouw,  
776 J., Hatch, L. E., Barsanti, K. C., and Brown, S. S.: Nighttime Chemical Transformation in Biomass  
777 Burning Plumes: A Box Model Analysis Initialized with Aircraft Observations, *Environmental Science  
778 & Technology*, 53, 2529-2538, 10.1021/acs.est.8b05359, 2019.

779 Donahue, N. M., Epstein, S. A., Pandis, S. N., and Robinson, A. L.: A two-dimensional volatility  
780 basis set: 1. organic-aerosol mixing thermodynamics, *Atmos. Chem. Phys.*, 11, 3303-3318, 10.5194/acp-  
781 11-3303-2011, 2011.

782 Donahue, N. M., Kroll, J. H., Pandis, S. N., and Robinson, A. L.: A two-dimensional volatility basis  
783 set – Part 2: Diagnostics of organic-aerosol evolution, *Atmos. Chem. Phys.*, 12, 615-634, 10.5194/acp-  
784 12-615-2012, 2012.

785 Faxon, C., Hammes, J., Le Breton, M., Pathak, R. K., and Hallquist, M.: Characterization of organic

786 nitrate constituents of secondary organic aerosol (SOA) from nitrate-radical-initiated oxidation of  
787 limonene using high-resolution chemical ionization mass spectrometry, *Atmos. Chem. Phys.*, 18, 5467-  
788 5481, 10.5194/acp-18-5467-2018, 2018.

789 Feng, T., Wang, Y., Hu, W., Zhu, M., Song, W., Chen, W., Sang, Y., Fang, Z., Deng, W., Fang, H.,  
790 Yu, X., Wu, C., Yuan, B., Huang, S., Shao, M., Huang, X., He, L., Lee, Y. R., Huey, L. G., Canonaco, F.,  
791 Prevot, A. S. H., and Wang, X.: Impact of aging on the sources, volatility, and viscosity of organic  
792 aerosols in Chinese outflows, *Atmos. Chem. Phys.*, 23, 611-636, 10.5194/acp-23-611-2023, 2023.

793 Fisher, J. A., Jacob, D. J., Travis, K. R., Kim, P. S., Marais, E. A., Chan Miller, C., Yu, K., Zhu, L.,  
794 Yantosca, R. M., Sulprizio, M. P., Mao, J., Wennberg, P. O., Crounse, J. D., Teng, A. P., Nguyen, T. B.,  
795 St. Clair, J. M., Cohen, R. C., Romer, P., Nault, B. A., Wooldridge, P. J., Jimenez, J. L., Campuzano-Jost,  
796 P., Day, D. A., Hu, W., Shepson, P. B., Xiong, F., Blake, D. R., Goldstein, A. H., Misztal, P. K., Hanisco,  
797 T. F., Wolfe, G. M., Ryerson, T. B., Wisthaler, A., and Mikoviny, T.: Organic nitrate chemistry and its  
798 implications for nitrogen budgets in an isoprene- and monoterpene-rich atmosphere: constraints from  
799 aircraft (SEAC4RS) and ground-based (SOAS) observations in the Southeast US, *Atmos. Chem. Phys.*,  
800 16, 5969-5991, 10.5194/acp-16-5969-2016, 2016.

801 Gaston, C. J., Lopez-Hilfiker, F. D., Whybrow, L. E., Hadley, O., McNair, F., Gao, H., Jaffe, D. A.,  
802 and Thornton, J. A.: Online molecular characterization of fine particulate matter in Port Angeles, WA:  
803 Evidence for a major impact from residential wood smoke, *Atmospheric Environment*, 138, 99-107,  
804 <https://doi.org/10.1016/j.atmosenv.2016.05.013>, 2016.

805 Graham, E. L., Wu, C., Bell, D. M., Bertrand, A., Haslett, S. L., Baltensperger, U., El Haddad, I.,  
806 Krejci, R., Riipinen, I., and Mohr, C.: Volatility of aerosol particles from NO<sub>3</sub> oxidation of various  
807 biogenic organic precursors, *Atmos. Chem. Phys.*, 23, 7347-7362, 10.5194/acp-23-7347-2023, 2023.

808 Guo, J., Zhou, S., Cai, M., Zhao, J., Song, W., Zhao, W., Hu, W., Sun, Y., He, Y., Yang, C., Xu, X.,  
809 Zhang, Z., Cheng, P., Fan, Q., Hang, J., Fan, S., Wang, X., and Wang, X.: Characterization of submicron  
810 particles by time-of-flight aerosol chemical speciation monitor (ToF-ACSM) during wintertime: aerosol  
811 composition, sources, and chemical processes in Guangzhou, China, *Atmos. Chem. Phys.*, 20, 7595-7615,  
812 10.5194/acp-20-7595-2020, 2020.

813 Hildebrandt Ruiz, L., Paciga, A. L., Cerully, K. M., Nenes, A., Donahue, N. M., and Pandis, S. N.:  
814 Formation and aging of secondary organic aerosol from toluene: changes in chemical composition,  
815 volatility, and hygroscopicity, *Atmos. Chem. Phys.*, 15, 8301-8313, 10.5194/acp-15-8301-2015, 2015.

816 Huang, R.-J., Zhang, Y., Bozzetti, C., Ho, K.-F., Cao, J.-J., Han, Y., Daellenbach, K. R., Slowik, J.  
817 G., Platt, S. M., Canonaco, F., Zotter, P., Wolf, R., Pieber, S. M., Bruns, E. A., Crippa, M., Ciarelli, G.,  
818 Piazzalunga, A., Schwikowski, M., Abbaszade, G., Schnelle-Kreis, J., Zimmermann, R., An, Z., Szidat,  
819 S., Baltensperger, U., Haddad, I. E., and Prevot, A. S. H.: High secondary aerosol contribution to  
820 particulate pollution during haze events in China, *Nature*, 514, 218-222, 10.1038/nature13774  
821 <http://www.nature.com/nature/journal/vaop/ncurrent/abs/nature13774.html#supplementary-information>, 2014.

822 Huang, S., Wu, Z., Poulain, L., van Pinxteren, M., Merkel, M., Assmann, D., Herrmann, H., and  
823 Wiedensohler, A.: Source apportionment of the organic aerosol over the Atlantic Ocean from  
824 53°N to 53°S: significant contributions from marine emissions and long-range transport,  
825 *Atmos. Chem. Phys.*, 18, 18043-18062, 10.5194/acp-18-18043-2018, 2018.

826 Huang, W., Saathoff, H., Shen, X., Ramisetty, R., Leisner, T., and Mohr, C.: Seasonal characteristics  
827 of organic aerosol chemical composition and volatility in Stuttgart, Germany, *Atmos. Chem. Phys.*, 19,  
828 11687-11700, 10.5194/acp-19-11687-2019, 2019.

830 Huang, X. F., He, L. Y., Hu, M., Canagaratna, M. R., Sun, Y., Zhang, Q., Zhu, T., Xue, L., Zeng, L.  
831 W., Liu, X. G., Zhang, Y. H., Jayne, J. T., Ng, N. L., and Worsnop, D. R.: Highly time-resolved chemical  
832 characterization of atmospheric submicron particles during 2008 Beijing Olympic Games using an  
833 Aerodyne High-Resolution Aerosol Mass Spectrometer, *Atmos. Chem. Phys.*, 10, 8933-8945,  
834 10.5194/acp-10-8933-2010, 2010.

835 Iyer, S., Lopez-Hilfiker, F., Lee, B. H., Thornton, J. A., and Kurtén, T.: Modeling the Detection of  
836 Organic and Inorganic Compounds Using Iodide-Based Chemical Ionization, *The Journal of Physical  
837 Chemistry A*, 120, 576-587, 10.1021/acs.jpca.5b09837, 2016.

838 Jenkin, M. E.: Modelling the formation and composition of secondary organic aerosol from  $\alpha$ - and  
839  $\beta$ -pinene ozonolysis using MCM v3, *Atmos. Chem. Phys.*, 4, 1741-1757, 10.5194/acp-4-1741-2004,  
840 2004.

841 Jimenez, J. L., Canagaratna, M., Donahue, N., Prevot, A., Zhang, Q., Kroll, J. H., DeCarlo, P. F.,  
842 Allan, J. D., Coe, H., and Ng, N. J. S.: Evolution of organic aerosols in the atmosphere, 326, 1525-1529,  
843 2009.

844 Jorga, S. D., Florou, K., Kaltsonoudis, C., Kodros, J. K., Vasilakopoulou, C., Cirtog, M., Fouqueau,  
845 A., Picquet-Varrault, B., Nenes, A., and Pandis, S. N.: Nighttime chemistry of biomass burning emissions  
846 in urban areas: A dual mobile chamber study, *Atmos. Chem. Phys.*, 21, 15337-15349, 10.5194/acp-21-  
847 15337-2021, 2021.

848 Kiendler-Scharr, A., Mensah, A. A., Fries, E., Topping, D., Nemitz, E., Prevot, A. S. H., Äijälä, M.,  
849 Allan, J., Canonaco, F., Canagaratna, M., Carbone, S., Crippa, M., Dall Osto, M., Day, D. A., De Carlo,  
850 P., Di Marco, C. F., Elbern, H., Eriksson, A., Freney, E., Hao, L., Herrmann, H., Hildebrandt, L., Hillamo,  
851 R., Jimenez, J. L., Laaksonen, A., McFiggans, G., Mohr, C., O'Dowd, C., Otjes, R., Ovadnevaite, J.,  
852 Pandis, S. N., Poulain, L., Schlag, P., Sellegri, K., Swietlicki, E., Tiitta, P., Vermeulen, A., Wahner, A.,  
853 Worsnop, D., and Wu, H. C.: Ubiquity of organic nitrates from nighttime chemistry in the European  
854 submicron aerosol, *Geophysical Research Letters*, 43, 7735-7744,  
855 <https://doi.org/10.1002/2016GL069239>, 2016.

856 Krieger, U. K., Siegrist, F., Marcolli, C., Emanuelsson, E. U., Gøbel, F. M., Bilde, M., Marsh, A.,  
857 Reid, J. P., Huisman, A. J., Riipinen, I., Hyttinen, N., Myllys, N., Kurtén, T., Bannan, T., Percival, C. J.,  
858 and Topping, D.: A reference data set for validating vapor pressure measurement techniques: homologous  
859 series of polyethylene glycols, *Atmos. Meas. Tech.*, 11, 49-63, 10.5194/amt-11-49-2018, 2018.

860 Kroll, J. H. and Seinfeld, J. H.: Chemistry of secondary organic aerosol: Formation and evolution  
861 of low-volatility organics in the atmosphere, *Atmospheric Environment*, 42, 3593-3624,  
862 <https://doi.org/10.1016/j.atmosenv.2008.01.003>, 2008.

863 Kuang, Y., Huang, S., Xue, B., Luo, B., Song, Q., Chen, W., Hu, W., Li, W., Zhao, P., Cai, M., Peng,  
864 Y., Qi, J., Li, T., Wang, S., Chen, D., Yue, D., Yuan, B., and Shao, M.: Contrasting effects of secondary  
865 organic aerosol formations on organic aerosol hygroscopicity, *Atmos. Chem. Phys.*, 21, 10375-10391,  
866 10.5194/acp-21-10375-2021, 2021.

867 [Lee, B. H., D'Ambro, E. L., Lopez-Hilfiker, F. D., Schobesberger, S., Mohr, C., Zawadowicz, M.  
868 A., Liu, J., Shilling, J. E., Hu, W., Palm, B. B., Jimenez, J. L., Hao, L., Virtanen, A., Zhang, H., Goldstein,  
869 A. H., Pye, H. O. T., and Thornton, J. A.: Resolving Ambient Organic Aerosol Formation and Aging  
870 Pathways with Simultaneous Molecular Composition and Volatility Observations, \*ACS Earth and Space  
871 Chemistry\*, 4, 391-402, 10.1021/acsearthspacechem.9b00302, 2020.](https://doi.org/10.1021/acsearthspacechem.9b00302)

872 Lee, B. H., Lopez-Hilfiker, F. D., Mohr, C., Kurtén, T., Worsnop, D. R., and Thornton, J. A.: An  
873 Iodide-Adduct High-Resolution Time-of-Flight Chemical-Ionization Mass Spectrometer: Application to

874 Atmospheric Inorganic and Organic Compounds, *Environmental Science & Technology*, 48, 6309-6317,  
875 10.1021/es500362a, 2014.

876 Lee, B. P., Li, Y. J., Yu, J. Z., Louie, P. K., and Chan, C. K.: Characteristics of submicron particulate  
877 matter at the urban roadside in downtown Hong Kong—Overview of 4 months of continuous high-  
878 resolution aerosol mass spectrometer measurements, *Journal of Geophysical Research: Atmospheres*,  
879 120, 7040-7058, 2015.

880 Lopez-Hilfiker, F. D., Iyer, S., Mohr, C., Lee, B. H., D'Ambro, E. L., Kurtén, T., and Thornton, J.  
881 A.: Constraining the sensitivity of iodide adduct chemical ionization mass spectrometry to  
882 multifunctional organic molecules using the collision limit and thermodynamic stability of iodide ion  
883 adducts, *Atmos. Meas. Tech.*, 9, 1505-1512, 10.5194/amt-9-1505-2016, 2016.

884 Lopez-Hilfiker, F. D., Mohr, C., Ehn, M., Rubach, F., Kleist, E., Wildt, J., Mentel, T. F., Lutz, A.,  
885 Hallquist, M., Worsnop, D., and Thornton, J. A.: A novel method for online analysis of gas and particle  
886 composition: description and evaluation of a Filter Inlet for Gases and AEROsols (FIGAERO), *Atmos.*  
887 *Meas. Tech.*, 7, 983-1001, 10.5194/amt-7-983-2014, 2014.

888 Louvaris, E. E., Florou, K., Karnezi, E., Papanastasiou, D. K., Gkatzelis, G. I., and Pandis, S. N.:  
889 Volatility of source apportioned wintertime organic aerosol in the city of Athens, *Atmospheric*  
890 *Environment*, 158, 138-147, <https://doi.org/10.1016/j.atmosenv.2017.03.042>, 2017.

891 Lu, Q., Murphy, B. N., Qin, M., Adams, P. J., Zhao, Y., Pye, H. O. T., Efstatthiou, C., Allen, C., and  
892 Robinson, A. L.: Simulation of organic aerosol formation during the CalNex study: updated mobile  
893 emissions and secondary organic aerosol parameterization for intermediate-volatility organic compounds,  
894 *Atmos. Chem. Phys.*, 20, 4313-4332, 10.5194/acp-20-4313-2020, 2020.

895 Matsui, H., Koike, M., Takegawa, N., Kondo, Y., Griffin, R. J., Miyazaki, Y., Yokouchi, Y., and  
896 Ohara, T.: Secondary organic aerosol formation in urban air: Temporal variations and possible  
897 contributions from unidentified hydrocarbons, *Journal of Geophysical Research: Atmospheres*, 114,  
898 <https://doi.org/10.1029/2008JD010164>, 2009.

899 Nie, W., Yan, C., Huang, D. D., Wang, Z., Liu, Y., Qiao, X., Guo, Y., Tian, L., Zheng, P., Xu, Z., Li,  
900 Y., Xu, Z., Qi, X., Sun, P., Wang, J., Zheng, F., Li, X., Yin, R., Dallenbach, K. R., Bianchi, F., Petäjä, T.,  
901 Zhang, Y., Wang, M., Schervish, M., Wang, S., Qiao, L., Wang, Q., Zhou, M., Wang, H., Yu, C., Yao, D.,  
902 Guo, H., Ye, P., Lee, S., Li, Y. J., Liu, Y., Chi, X., Kerminen, V.-M., Ehn, M., Donahue, N. M., Wang, T.,  
903 Huang, C., Kulmala, M., Worsnop, D., Jiang, J., and Ding, A.: Secondary organic aerosol formed by  
904 condensing anthropogenic vapours over China's megacities, *Nature Geoscience*, 15, 255-261,  
905 10.1038/s41561-022-00922-5, 2022.

906 Nie, W., Yan, C., Yang, L., Roldin, P., Liu, Y., Vogel, A. L., Molteni, U., Stolzenburg, D.,  
907 Finkenzeller, H., Amorim, A., Bianchi, F., Curtius, J., Dada, L., Draper, D. C., Duplissy, J., Hansel, A.,  
908 He, X.-C., Hofbauer, V., Jokinen, T., Kim, C., Lehtipalo, K., Nichman, L., Mauldin, R. L., Makhmutov,  
909 V., Mentler, B., Mizelli-Ojadic, A., Petäjä, T., Quéléver, L. L. J., Schallhart, S., Simon, M., Tauber, C.,  
910 Tomé, A., Volkamer, R., Wagner, A. C., Wagner, R., Wang, M., Ye, P., Li, H., Huang, W., Qi, X., Lou, S.,  
911 Liu, T., Chi, X., Dommen, J., Baltensperger, U., El Haddad, I., Kirkby, J., Worsnop, D., Kulmala, M.,  
912 Donahue, N. M., Ehn, M., and Ding, A.: NO at low concentration can enhance the formation of highly  
913 oxygenated biogenic molecules in the atmosphere, *Nature Communications*, 14, 3347, 10.1038/s41467-  
914 023-39066-4, 2023.

915 Nihill, K. J., Ye, Q., Majluf, F., Krechmer, J. E., Canagaratna, M. R., and Kroll, J. H.: Influence of  
916 the NO/NO<sub>2</sub> Ratio on Oxidation Product Distributions under High-NO Conditions, *Environmental*  
917 *Science & Technology*, 55, 6594-6601, 10.1021/acs.est.0c07621, 2021.

918        Ou, H. J., Cai, M. F., Liang, B. L., Sun, Q. B., Zhou, S. Z., Xu, Y. S., Ren, L. H., and Zhao, J.:  
919        Characterization, Sources, and Chemical Processes of Submicron Aerosols at a Mountain Site in Central  
920        China, *Journal of Geophysical Research: Atmospheres*, 128, e2022JD038258,  
921        <https://doi.org/10.1029/2022JD038258>, 2023.

922        Paatero, P. and Tapper, U.: Positive matrix factorization: A non-negative factor model with optimal  
923        utilization of error estimates of data values, *Environmetrics*, 5, 111-126,  
924        <https://doi.org/10.1002/env.3170050203>, 1994.

925        Paulot, F., Crounse, J. D., Kjaergaard, H. G., Kroll, J. H., Seinfeld, J. H., and Wennberg, P. O.:  
926        Isoprene photooxidation: new insights into the production of acids and organic nitrates, *Atmos. Chem.*  
927        *Phys.*, 9, 1479-1501, 10.5194/acp-9-1479-2009, 2009.

928        Praske, E., Otkjær, R. V., Crounse, J. D., Hethcox, J. C., Stoltz, B. M., Kjaergaard, H. G., and  
929        Wennberg, P. O.: Atmospheric autoxidation is increasingly important in urban and suburban North  
930        America, *Proceedings of the National Academy of Sciences*, 115, 64-69, 10.1073/pnas.1715540115,  
931        2018.

932        Pye, H. O. T., D'Ambro, E. L., Lee, B. H., Schobesberger, S., Takeuchi, M., Zhao, Y., Lopez-Hilfiker,  
933        F., Liu, J., Shilling, J. E., Xing, J., Mathur, R., Middlebrook, A. M., Liao, J., Welti, A., Graus, M.,  
934        Warneke, C., de Gouw, J. A., Holloway, J. S., Ryerson, T. B., Pollack, I. B., and Thornton, J. A.:  
935        Anthropogenic enhancements to production of highly oxygenated molecules from autoxidation,  
936        *Proceedings of the National Academy of Sciences*, 116, 6641-6646, 10.1073/pnas.1810774116, 2019.

937        Qin, Y. M., Tan, H. B., Li, Y. J., Schurman, M. I., Li, F., Canonaco, F., Prévôt, A. S. H., and Chan,  
938        C. K.: The role of traffic emissions in particulate organics and nitrate at a downwind site in the periphery  
939        of Guangzhou, China, *Atmospheric Chemistry & Physics*, 1-31, 2017.

940        Ren, S., Yao, L., Wang, Y., Yang, G., Liu, Y., Li, Y., Lu, Y., Wang, L., and Wang, L.: Volatility  
941        parameterization of ambient organic aerosols at a rural site of the North China Plain, *Atmos. Chem. Phys.*,  
942        22, 9283-9297, 10.5194/acp-22-9283-2022, 2022.

943        Rissanen, M. P.: NO<sub>2</sub> Suppression of Autoxidation-Inhibition of Gas-Phase Highly Oxidized Dimer  
944        Product Formation, *ACS Earth and Space Chemistry*, 2, 1211-1219,  
945        10.1021/acsearthspacechem.8b00123, 2018.

946        Rudich, Y., Donahue, N. M., and Mentel, T. F.: Aging of Organic Aerosol: Bridging the Gap  
947        Between Laboratory and Field Studies, *Annual Review of Physical Chemistry*, 58, 321-352,  
948        <https://doi.org/10.1146/annurev.physchem.58.032806.104432>, 2007.

949        Shrivastava, M., Andreae, M. O., Artaxo, P., Barbosa, H. M. J., Berg, L. K., Brito, J., Ching, J.,  
950        Easter, R. C., Fan, J., Fast, J. D., Feng, Z., Fuentes, J. D., Glasius, M., Goldstein, A. H., Alves, E. G.,  
951        Gomes, H., Gu, D., Guenther, A., Jathar, S. H., Kim, S., Liu, Y., Lou, S., Martin, S. T., McNeill, V. F.,  
952        Medeiros, A., de Sá, S. S., Shilling, J. E., Springston, S. R., Souza, R. A. F., Thornton, J. A., Isaacman-  
953        VanWertz, G., Yee, L. D., Ynoue, R., Zaveri, R. A., Zelenyuk, A., and Zhao, C.: Urban pollution greatly  
954        enhances formation of natural aerosols over the Amazon rainforest, *Nature Communications*, 10, 1046,  
955        10.1038/s41467-019-08909-4, 2019.

956        Thornton, J. A., Mohr, C., Schobesberger, S., D'Ambro, E. L., Lee, B. H., and Lopez-Hilfiker, F. D.:  
957        Evaluating Organic Aerosol Sources and Evolution with a Combined Molecular Composition and  
958        Volatility Framework Using the Filter Inlet for Gases and Aerosols (FIGAERO), *Accounts of Chemical*  
959        *Research*, 53, 1415-1426, 10.1021/acs.accounts.0c00259, 2020.

960        Tian, S. L., Pan, Y. P., and Wang, Y. S.: Size-resolved source apportionment of particulate matter in  
961        urban Beijing during haze and non-haze episodes, *Atmos. Chem. Phys.*, 16, 1-19, 10.5194/acp-16-1-2016,

962 2016.  
963 Ulbrich, I. M., Canagaratna, M. R., Zhang, Q., Worsnop, D. R., and Jimenez, J. L.: Interpretation of  
964 organic components from Positive Matrix Factorization of aerosol mass spectrometric data, *Atmos.*  
965 *Chem. Phys.*, 9, 2891-2918, 10.5194/acp-9-2891-2009, 2009.  
966 Walser, M. L., Park, J., Gomez, A. L., Russell, A. R., and Nizkorodov, S. A.: Photochemical Aging  
967 of Secondary Organic Aerosol Particles Generated from the Oxidation of d-Limonene, *The Journal of*  
968 *Physical Chemistry A*, 111, 1907-1913, 10.1021/jp0662931, 2007.  
969 Wang, Y., Clusius, P., Yan, C., Dällenbach, K., Yin, R., Wang, M., He, X.-C., Chu, B., Lu, Y., Dada,  
970 L., Kangasluoma, J., Rantala, P., Deng, C., Lin, Z., Wang, W., Yao, L., Fan, X., Du, W., Cai, J., Heikkinen,  
971 L., Tham, Y. J., Zha, Q., Ling, Z., Junninen, H., Petäjä, T., Ge, M., Wang, Y., He, H., Worsnop, D. R.,  
972 Kermoisen, V.-M., Bianchi, F., Wang, L., Jiang, J., Liu, Y., Boy, M., Ehn, M., Donahue, N. M., and  
973 Kulmala, M.: Molecular Composition of Oxygenated Organic Molecules and Their Contributions to  
974 Organic Aerosol in Beijing, *Environmental Science & Technology*, 56, 770-778,  
975 10.1021/acs.est.1c05191, 2022.  
976 Ulbrich, I. M., Canagaratna, M. R., Zhang, Q., Worsnop, D. R., and Jimenez, J. L.: Interpretation of  
977 organic components from Positive Matrix Factorization of aerosol mass spectrometric data, *Atmos.*  
978 *Chem. Phys.*, 9, 2891-2918, 10.5194/acp-9-2891-2009, 2009.  
979 Uchida, K., Ide, Y., and Takegawa, N.: Ionization efficiency of evolved gas molecules from aerosol  
980 particles in a thermal desorption aerosol mass spectrometer: Laboratory experiments, *Aerosol Sci Tech*,  
981 53, 86-93, 10.1080/02786826.2018.1544704, 2019.  
982 Wu, C., Bell, D. M., Graham, E. L., Haslett, S., Riipinen, I., Baltensperger, U., Bertrand, A.,  
983 Giannoukos, S., Schoonbaert, J., El Haddad, I., Prevot, A. S. H., Huang, W., and Mohr, C.: Photolytically  
984 induced changes in composition and volatility of biogenic secondary organic aerosol from nitrate radical  
985 oxidation during night-to-day transition, *Atmos. Chem. Phys.*, 21, 14907-14925, 10.5194/acp-21-14907-  
986 2021, 2021.  
987 Xu, L., Kollman, M. S., Song, C., Shilling, J. E., and Ng, N. L.: Effects of NO<sub>x</sub> on the Volatility of  
988 Secondary Organic Aerosol from Isoprene Photooxidation, *Environmental Science & Technology*, 48,  
989 2253-2262, 10.1021/es404842g, 2014.  
990 Xu, W., Chen, C., Qiu, Y., Li, Y., Zhang, Z., Karnezi, E., Pandis, S. N., Xie, C., Li, Z., Sun, J., Ma,  
991 N., Xu, W., Fu, P., Wang, Z., Zhu, J., Worsnop, D. R., Ng, N. L., and Sun, Y.: Organic aerosol volatility  
992 and viscosity in the North China Plain: contrast between summer and winter, *Atmos. Chem. Phys.*, 21,  
993 5463-5476, 10.5194/acp-21-5463-2021, 2021.  
994 Xu, X., Wang, G., Gao, Y., Zhang, S., Chen, L., Li, R., Li, Z., and Li, R.: Smog chamber study on  
995 the NO<sub>x</sub> dependence of SOA from isoprene photo-oxidation: implication on RO<sub>2</sub> chemistry, *Journal of*  
996 *Environmental Sciences*, <https://doi.org/10.1016/j.jes.2025.05.024>, 2025.  
997 Xu, W., Xie, C., Karnezi, E., Zhang, Q., Wang, J., Pandis, S. N., Ge, X., Zhang, J., An, J., Wang, Q.,  
998 Zhao, J., Du, W., Qiu, Y., Zhou, W., He, Y., Li, Y., Li, J., Fu, P., Wang, Z., Worsnop, D. R., and Sun, Y.:  
999 Summertime aerosol volatility measurements in Beijing, China, *Atmos. Chem. Phys.*, 19, 10205-10216,  
1000 10.5194/acp-19-10205-2019, 2019.  
1001 Xu, W., Chen, C., Qiu, Y., Li, Y., Zhang, Z., Karnezi, E., Pandis, S. N., Xie, C., Li, Z., Sun, J., Ma,  
1002 N., Xu, W., Fu, P., Wang, Z., Zhu, J., Worsnop, D. R., Ng, N. L., and Sun, Y.: Organic aerosol volatility  
1003 and viscosity in the North China Plain: contrast between summer and winter, Atmos. Chem. Phys., 21,  
1004 5463-5476, 10.5194/acp-21-5463-2021, 2021.  
1005 Yang, S., Yuan, B., Peng, Y., Huang, S., Chen, W., Hu, W., Pei, C., Zhou, J., Parrish, D. D., Wang,

1006 W., He, X., Cheng, C., Li, X. B., Yang, X., Song, Y., Wang, H., Qi, J., Wang, B., Wang, C., Wang, C.,  
1007 Wang, Z., Li, T., Zheng, E., Wang, S., Wu, C., Cai, M., Ye, C., Song, W., Cheng, P., Chen, D., Wang, X.,  
1008 Zhang, Z., Wang, X., Zheng, J., and Shao, M.: The formation and mitigation of nitrate pollution:  
1009 comparison between urban and suburban environments, *Atmos. Chem. Phys.*, 22, 4539-4556,  
1010 10.5194/acp-22-4539-2022, 2022.

1011 Ye, C., Liu, Y., Yuan, B., Wang, Z., Lin, Y., Hu, W., Chen, W., Li, T., Song, W., Wang, X., Lv, D.,  
1012 Gu, D., and Shao, M.: Low-NO-like Oxidation Pathway Makes a Significant Contribution to Secondary  
1013 Organic Aerosol in Polluted Urban Air, *Environmental Science & Technology*, 10.1021/acs.est.3c01055,  
1014 2023.

1015 Ye, C., Yuan, B., Lin, Y., Wang, Z., Hu, W., Li, T., Chen, W., Wu, C., Wang, C., Huang, S., Qi, J.,  
1016 Wang, B., Wang, C., Song, W., Wang, X., Zheng, E., Krechmer, J. E., Ye, P., Zhang, Z., Wang, X.,  
1017 Worsnop, D. R., and Shao, M.: Chemical characterization of oxygenated organic compounds in the gas  
1018 phase and particle phase using iodide CIMS with FIGAERO in urban air, *Atmos. Chem. Phys.*, 21, 8455-  
1019 8478, 10.5194/acp-21-8455-2021, 2021.

1020 Ylisirniö, A., Barreira, L. M. F., Pullinen, I., Buchholz, A., Jayne, J., Krechmer, J. E., Worsnop, D.  
1021 R., Virtanen, A., and Schobesberger, S.: On the calibration of FIGAERO-ToF-CIMS: importance and  
1022 impact of calibrant delivery for the particle-phase calibration, *Atmos. Meas. Tech.*, 14, 355-367,  
1023 10.5194/amt-14-355-2021, 2021.

1024 [Ylisirniö, A., Hyttinen, N., Li, Z., Alton, M., Nissinen, A., Pullinen, I., Miettinen, P., Yli-Juuti, T.,  
1025 and Schobesberger, S.: The saturation vapor pressures of higher-order polyethylene glycols and  
1026 achieving a wide calibration range for volatility measurements by FIGAERO-CIMS, Atmos. Meas. Tech.,  
1027 18, 6449-6464, 10.5194/amt-18-6449-2025, 2025.](#)

1028 Zhang, Q., Jimenez, J. L., Canagaratna, M. R., Ulbrich, I. M., Ng, N. L., Worsnop, D. R., and Sun,  
1029 Y.: Understanding atmospheric organic aerosols via factor analysis of aerosol mass spectrometry: a  
1030 review, *Analytical and Bioanalytical Chemistry*, 401, 3045-3067, 10.1007/s00216-011-5355-y, 2011.

1031 Zhang, Y. L., El-Haddad, I., Huang, R. J., Ho, K. F., Cao, J. J., Han, Y., Zotter, P., Bozzetti, C.,  
1032 Daellenbach, K. R., Slowik, J. G., Salazar, G., Prévôt, A. S. H., and Szidat, S.: Large contribution of  
1033 fossil fuel derived secondary organic carbon to water soluble organic aerosols in winter haze in China,  
1034 *Atmos. Chem. Phys.*, 18, 4005-4017, 10.5194/acp-18-4005-2018, 2018.

1035 Zhao, W., Kawamura, K., Yue, S., Wei, L., Ren, H., Yan, Y., Kang, M., Li, L., Ren, L., Lai, S., Li,  
1036 J., Sun, Y., Wang, Z., and Fu, P.: Molecular distribution and compound-specific stable carbon isotopic  
1037 composition of dicarboxylic acids, oxocarboxylic acids and  $\alpha$ -dicarbonyls in PM2.5 from Beijing, China,  
1038 *Atmos. Chem. Phys.*, 18, 2749-2767, 10.5194/acp-18-2749-2018, 2018.

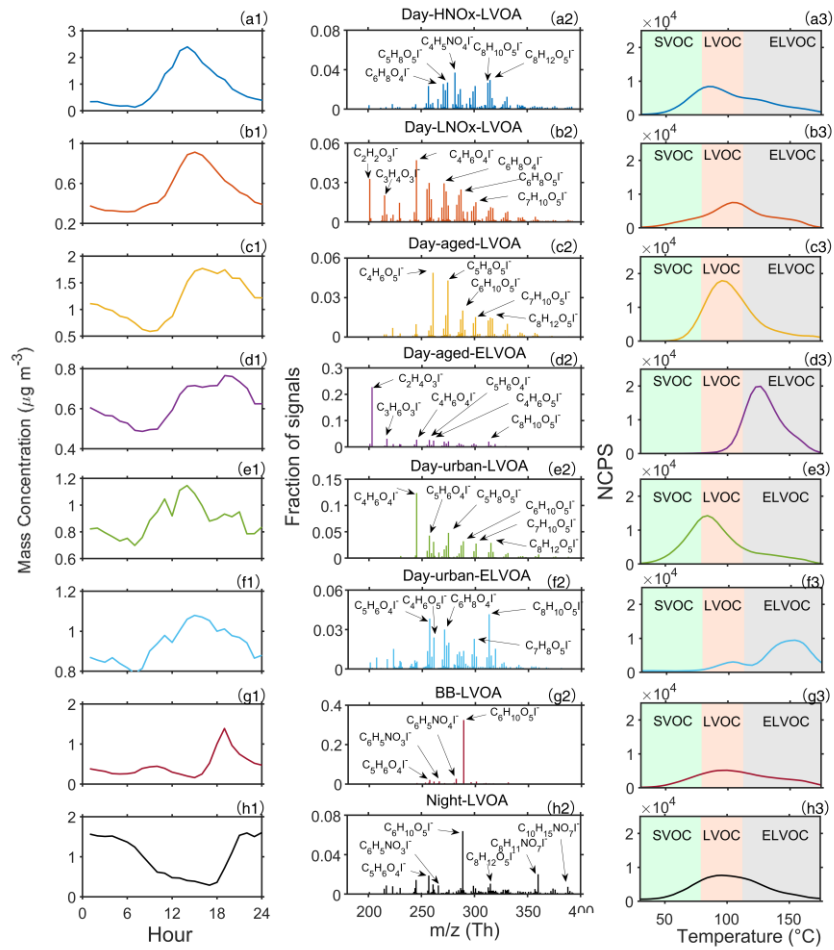
1039 Zheng, Y., Chen, Q., Cheng, X., Mohr, C., Cai, J., Huang, W., Shrivastava, M., Ye, P., Fu, P., Shi,  
1040 X., Ge, Y., Liao, K., Miao, R., Qiu, X., Koenig, T. K., and Chen, S.: Precursors and Pathways Leading to  
1041 Enhanced Secondary Organic Aerosol Formation during Severe Haze Episodes, *Environmental Science  
1042 & Technology*, 10.1021/acs.est.1c04255, 2021.

1043 Zhou, W., Xu, W., Kim, H., Zhang, Q., Fu, P., Worsnop, D. R., and Sun, Y.: A review of aerosol  
1044 chemistry in Asia: insights from aerosol mass spectrometer measurements, *Environmental Science:  
1045 Processes & Impacts*, 22, 1616-1653, 10.1039/D0EM00212G, 2020.

1046 **Table 1.** The average volatility ( $\log_{10} \overline{C^*}$ ),  $T_{max}$ , signal-weighted average values of elemental  
 1047 composition, carbon oxidation state ( $\overline{OS_c}$ ), H:C, O:C, N:C for all FIGAERO-OA factors. The  
 1048 estimation of  $\overline{OS_c}$  can be found in Section S2. The volatility of each FIGAERO-OA factor was  
 1049 estimated based on their corresponding  $T_{max}$  using eq. (8) and (9).

	$\log_{10} \overline{C^*}$ ( $\mu\text{g m}^{-3}$ )	$T_{max}$ (°C)	<u>Average elemental</u> <u>cE</u> omposition	$\overline{OS_c}$	H:C	O:C	N:C
Day-HNO <sub>x</sub> - LVOA	-0.98	84.52	$\text{C}_{7.37}\text{H}_{10.51}\text{O}_{4.99}\text{N}_{0.36}$	-0.01	1.37	0.75	0.06
Day-LNO <sub>x</sub> - LVOA	-2.71	103.29	$\text{C}_{6.52}\text{H}_{8.77}\text{O}_{4.54}\text{N}_{0.22}$	0.18	1.35	0.80	0.04
Day-aged- LVOA	-2.02	95.53	$\text{C}_{6.35}\text{H}_{8.75}\text{O}_{5.13}\text{N}_{0.21}$	0.35	1.42	0.91	0.04
Day-aged- ELVOA	-4.80	126.65	$\text{C}_{5.22}\text{H}_{7.36}\text{O}_{4.20}\text{N}_{0.16}$	0.40	1.55	1.00	0.03
Day-urban- LVOA	-0.90	83.03	$\text{C}_{6.50}\text{H}_{9.27}\text{O}_{4.71}\text{N}_{0.24}$	0.08	1.43	0.80	0.04
Day-urban- ELVOA	-7.18	153.22	$\text{C}_{6.57}\text{H}_{8.54}\text{O}_{4.61}\text{N}_{0.24}$	0.26	1.35	0.84	0.05
BB-LVOA	-2.36	99.39	$\text{C}_{6.72}\text{H}_{9.78}\text{O}_{4.61}\text{N}_{0.26}$	-0.08	1.47	0.74	0.04
Night-LVOA	-2.02	95.53	$\text{C}_{7.69}\text{H}_{11.04}\text{O}_{5.19}\text{N}_{0.47}$	-0.09	1.47	0.77	0.07

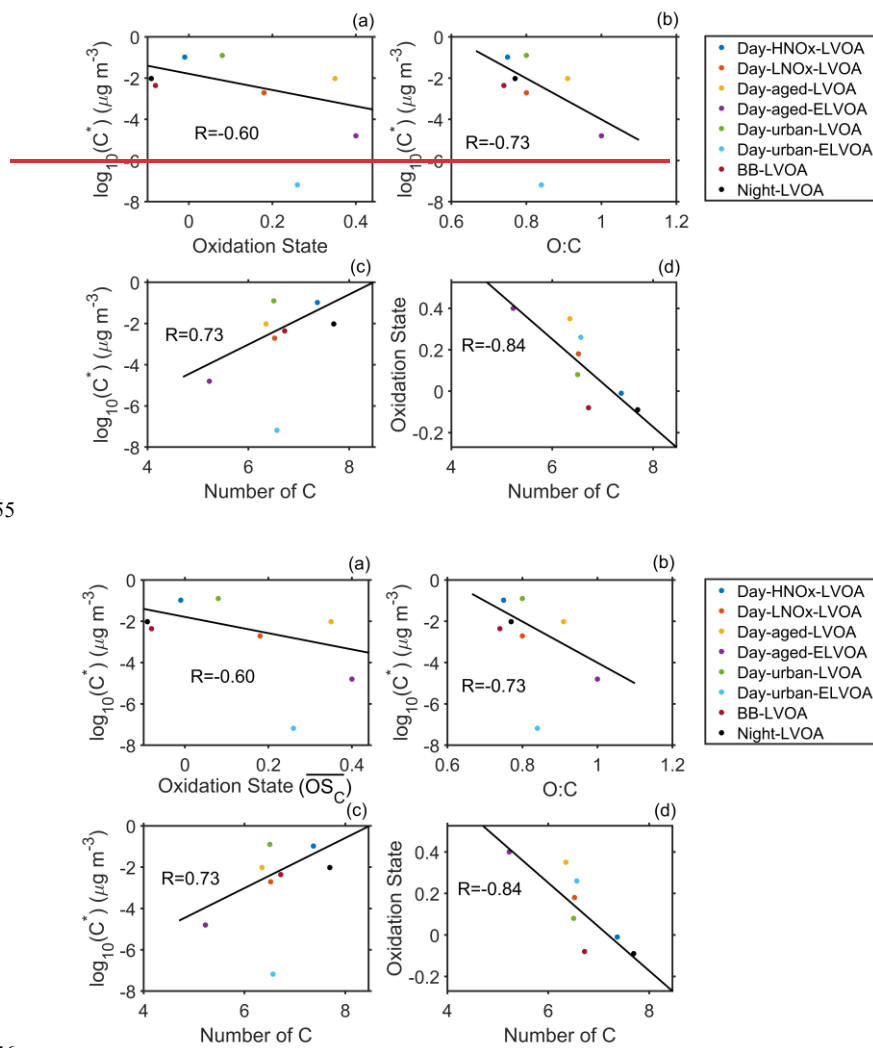
1050



1051

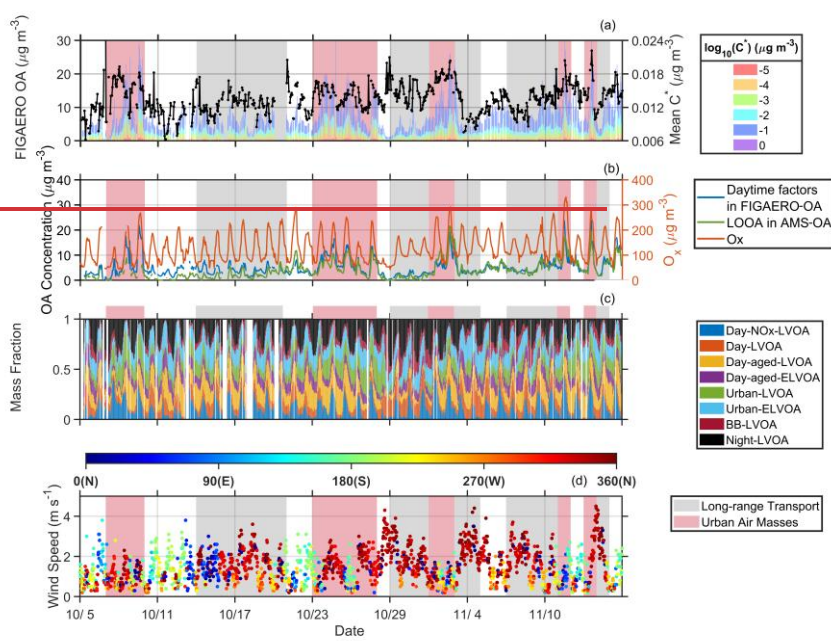
1052 **Figure 1.** Diurnal variation (a1 to h1), mass spectra (a2 to h2), and thermograms (a3 to h3) of  
1053 FIGAERO-OA factors.

1054

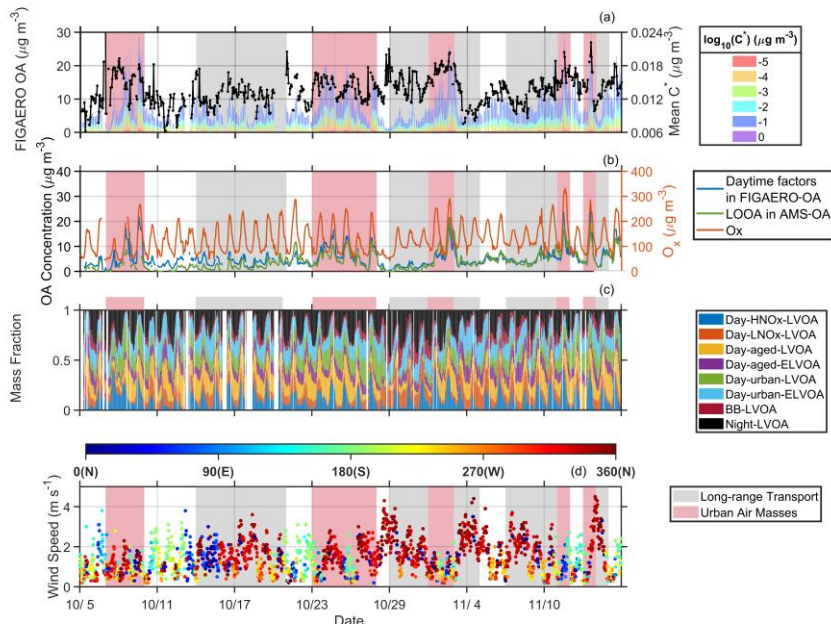


1057 **Figure 2.** The average volatility of FIGAERO-OA factor vs. (a) oxidation state ( $\overline{OS_c}$ ), (b) O:C ,  
 1058 and (c) number of carbons and (d) Number of carbons vs.  $\overline{OS_c}$  of thermogram factor. Day-urban-  
 1059 ELVOA is excluded in the estimation of R.

1061



1062



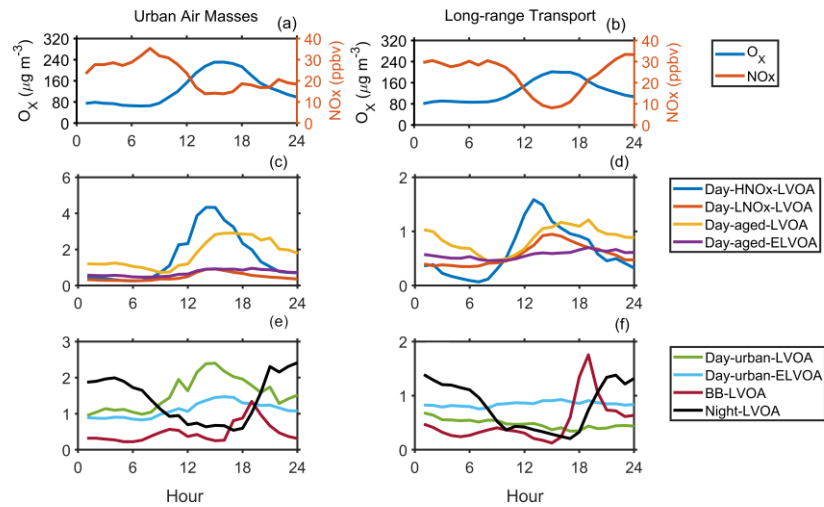
1063

1064 **Figure 3.** Time series of (a) volatility (presented in a range from  $10^{-5}$  to  $10^0 \mu\text{g m}^{-3}$ ) of FIGAERO-

1065 OA and mean  $C^*$ , (b) daytime factors (Day-HNO<sub>x</sub>-LVOA, Day-LNO<sub>x</sub>-LVOA, Day-aged-LVOA,  
1066 Day-aged-ELVOA, Urban LVOA, and Day-urban-ELVOA) in FIGAERO-OA and LOOA factor  
1067 from PMF analysis of SP-AMS data, (c) mass fraction of eight FIGAERO-OA factors, and (d) wind  
1068 speed and wind direction.

1069

1070

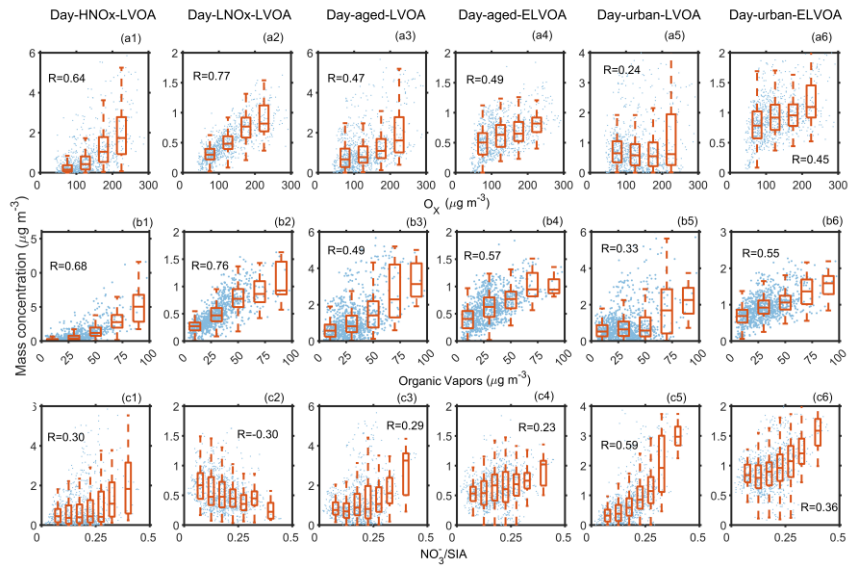


1071

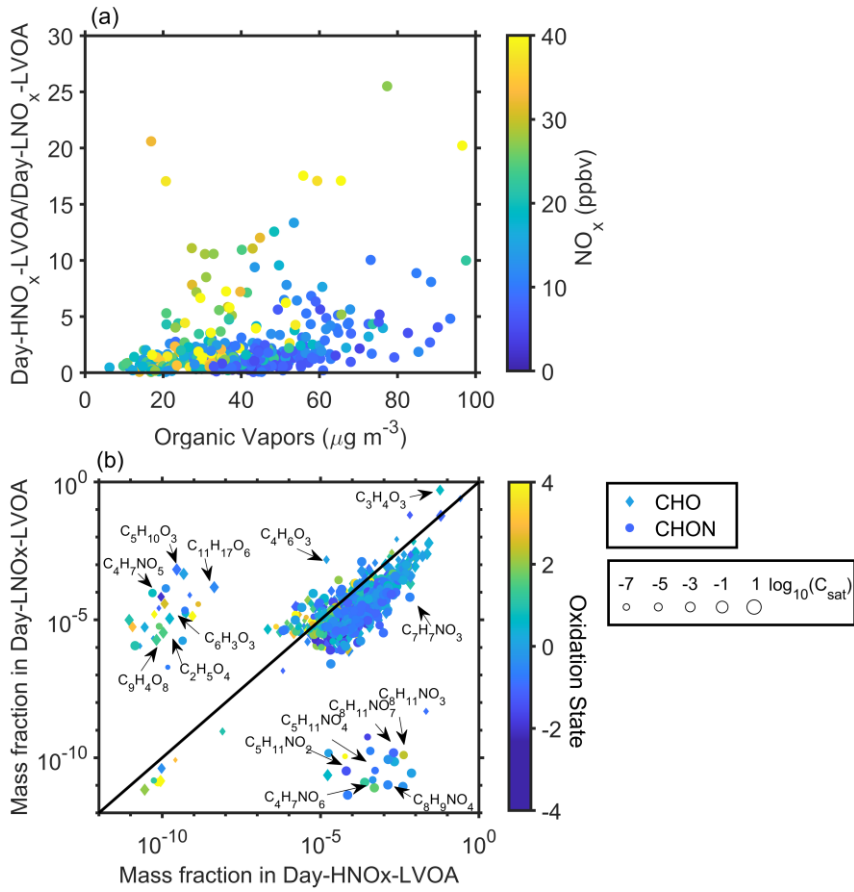
1072 **Figure 4.** The average diurnal variation of  $O_x$ ,  $NO_x$ , and mass concentration of eight thermogram

1073 factors during the long-range transport (a, c, and e) and urban air masses (b, d, and f) period.

1074



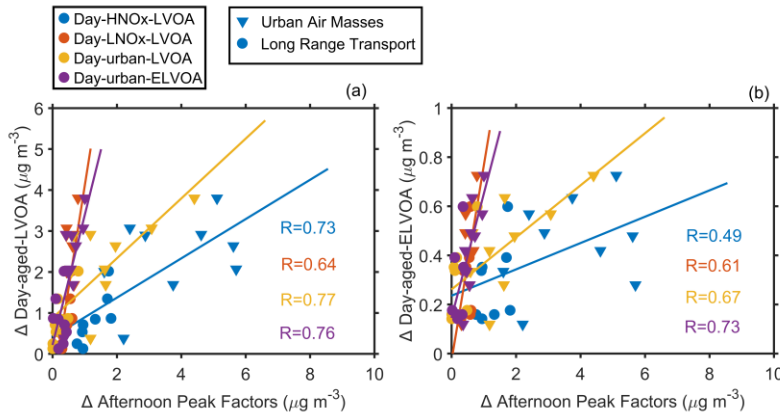
1077 **Figure 5.** Relationship between the mass concentration of six daytime thermogram factors and  
1078 (a1-6)  $O_x$ , (b1-6) organic vapors, (c1-6) nitrate fraction in secondary inorganic aerosol (SIA), and  
1079 (d1-6) sulfate fraction in SIA measured by the FIGAERO-CIMS. The organic vapors are the sum  
1080 of organic compounds in the gas-phase measured by the FIGAERO-CIMS.



1082

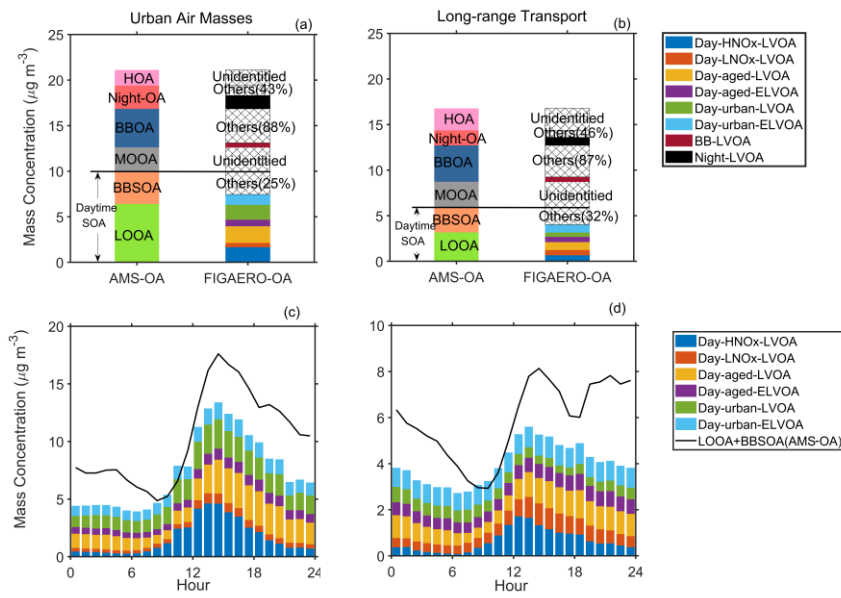
1083 **Figure 6.** (a) Correlation between organic vapors and the ratio of Day-HNO<sub>x</sub>-LVOA to Day-LNO<sub>x</sub>-  
1084 LVOA. (b) Scatterplots of mass fraction of different species in Day-HNO<sub>x</sub>-LVOA and Day-LNO<sub>x</sub>-  
1085 LVOA. The color of dots in panel (a) denotes the corresponding NO<sub>x</sub>. The shape, size, and color of  
1086 markers in panel (b) represents the class of species, volatility, and  $\overline{OS}_C$ , respectively.

1087



1090 **Figure 7.** Correlation between the enhancement of (a) Day-aged-LVOA and afternoon peak factors  
1091 and (b) Day-aged-ELVOA and afternoon peak factors. Afternoon peak factors include Day-HNO<sub>x</sub>-  
1092 LVOA, Day-LNO<sub>x</sub>-LVOA, Day-urban-LVOA, and Day-urban-ELVOA. For afternoon peak factors,  
1093 the enhancement ( $\Delta$ ) was regarded as the average mass concentration during 00:00-6:00 LT and  
1094 12:00-18:00 LT. For Day-aged-LVOA and Day-aged-ELVOA, the enhancement ( $\Delta$ ) was estimated  
1095 as the difference between average mass concentration during 00:00-6:00 LT and 12:00-18:00 LT.  
1096

1097

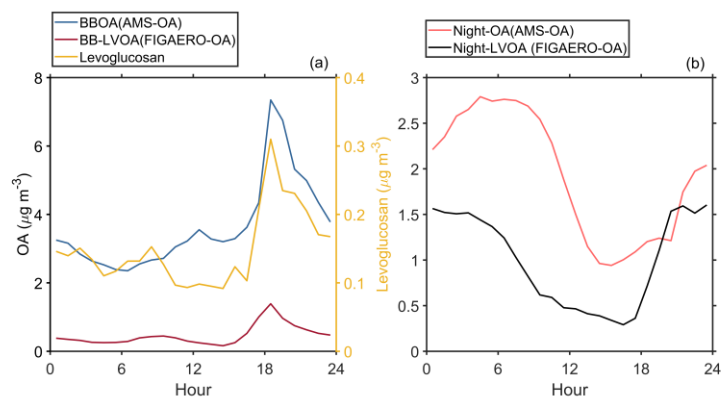


1098

1099 **Figure 8.** Comparison of the average mass concentration (a and b) and diurnal variation (c and d)  
1100 of AMS-OA and FIGAERO-OA during long-range transport and urban air masses period.

1101

1102



1103

1104 **Figure 9. (a)** Diurnal variation of BBOA from AMS, BB-LVOA and levoglucosan from FIGAERO-

1105 CIMS;(b) Diurnal variation of Night-OA from AMS, and Night-LVOA from FIGAERO-CIMS.

1106

1107